The Astrophysical Journal, 972:132 (17pp), 2024 September 10 https://doi.org/10.3847/1538-4357/ad5f93

GRB 231129C: Another Thermal Emission Dominated Gamma-Ray Burst

Jia-Ming Chen[1], Ke-Rui Zhu[1], Zhao-Yang Peng[2], and Li Zhang[1]
[1] Department of Astronomy, School of Physics and Astronomy, Key Laboratory of Astroparticle Physics of Yunnan Province, Yunnan University, Kunming 650091, People's Republic of China; lizhang@ynu.edu.cn
[2] College of Physics and Electronics, Yunnan Normal University, Kunming 650500, People's Republic of China
Received 2024 March 25; revised 2024 June 30; accepted 2024 July 3; published 2024 September 2

Abstract

This study presents detailed time-integrated and time-resolved spectral analysis of the Fermi Gamma-ray Burst Monitor observations of the bright GRB 231129C. The results reveal its distinct spectral characteristics, featuring a hard low-energy spectral index (α) and soft high-energy spectral index (β), similar to GRB 090902B, suggesting a possible dominance of thermal emission. Further analysis indicates that 92% of the spectral indices exceed the synchrotron "line of death," with the hardest index at $\alpha \sim +0.44$. Simultaneously, 53% of the spectra can be well fitted by the nondissipative photosphere model, supporting a potential origin from a nondissipative photosphere. Additionally, we observe strong correlations between the spectral index α and peak energy $E_{\rm p}$ with flux. For the $\alpha-F$ relationship, we employ $F = F_0 e^{(3.00\pm0.10)\,\alpha}$ to describe it, whereas the $E_{\rm p}-F$ relationship requires a smoothly bending power-law function. Based on the framework proposed by Hascoët et al. and Gao & Zhang, the jet characteristics of this burst were studied, revealing that both methods support the suitability of a pure fireball model for this GRB at small initial jet radii.

Unified Astronomy Thesaurus concepts: Gamma-ray bursts (629)

1. Introduction

Gamma-ray bursts (GRBs) are among the most intense and highly energetic phenomena in the universe. The rapid advancement of astronomical observation technologies over the past decades has led to a significant leap in our understanding of the prompt emission characteristics of GRBs. Within the widely used fireball model, energy is initially released in the form of a hot plasma composed of electron–positron pairs, photons, and baryons (Goodman 1986; Paczynski 1990; Shemi & Piran 1990; Paczyński 1998), which is then accelerated to relativistic speeds (Meszaros & Rees 1993; Piran et al. 1993). Despite substantial progress in our understanding of GRBs, the nature of their prompt emission mechanism remains uncertain (Kumar & Zhang 2015; Zhang 2018, 2020; Mészáros 2019). In the fireball model, thermal emission is released when the jet becomes optically thin at the photosphere layer (Mészáros & Rees 2000; Kobayashi et al. 2002), and this photospheric emission plays a dominant role within the standard framework of the model (Zhang & Pe'er 2009). However, most GRB spectra observed during the Compton Gamma Ray Observatory/BATSE era exhibit nonthermal characteristics, which can be effectively fitted by the so-called "Band" function (Band et al. 1993, an empirical function with smoothly joined break points in a power-law distribution). These nonthermal spectra are typically explained by the standard internal shock model (Rees & Meszaros 1994). In the internal shock model, a portion of the kinetic energy carried by the GRB ejecta is converted into internal energy, which is then released as radiation through nonthermal mechanisms such as synchrotron radiation or inverse Compton (IC) scattering. However, the internal shock model faces several major challenges, such as low radiation efficiency (Kumar 1999) and the so-called fast cooling problem (Ghisellini et al. 2000). To address the efficiency issue, extreme conditions are required (Kobayashi & Sari 2001). Another widely studied alternative is the magnetic dissipation model, such as the Internal-Collision-Induced Magnetic Reconnection and Turbulence model (Zhang & Yan 2011), which provides solutions to the problems encountered by the internal shock model. To resolve the fast cooling problem, researchers have explored additional effects such as IC cooling, the Klein–Nishina effect, magnetic field decay, and adiabatic cooling to comprehensively explain the observed GRB spectra (Asano & Terasawa 2009; Wang et al. 2009; Daigne et al. 2011; Uhm & Zhang 2014; Geng et al. 2018). The low-energy spectral index derived from the Band function is useful in assessing whether the limit of optically thin synchrotron emission has been exceeded (Preece et al. 2002; Ghirlanda et al. 2003). For GRBs exceeding this limit, the incorporation of thermal spectra, usually described by a Planck function, needs to be considered (Ryde 2004; Ryde & Pe'er 2009; Iyyani et al. 2015, 2016).

Observations by BATSE have confirmed the presence of a quasi-thermal component (Ryde et al. 2005; Ryde & Pe'er 2009). With the advent of the Fermi era, further observations have revealed this potential component in some events, such as GRB 100724B (Guiriec et al. 2011), GRB 100507 (Ghirlanda et al. 2013), GRB 120323A (Guiriec et al. 2013, 2017), and GRB 210610B (Chen et al. 2022). In some of these bursts, the primary thermal component is weak, with only partial blackbody (BB) spectra observable. A subdominant BB component, superimposed on the Band function, has been observed in numerous GRB cases. In GRBs with identified thermal components, it is more common for the thermal component to be subdominant, suggesting that many GRBs may have magnetized outflows. Furthermore, the diversity of observations indicates that the composition of jets may vary with each GRB, also proposing the possibility of a hybrid jet model that includes both thermal and magnetic components. Such a model may be more plausible (Guiriec et al. 2011; Hascoët et al. 2013; Gao & Zhang 2015; Li 2020; Chen et al. 2022).

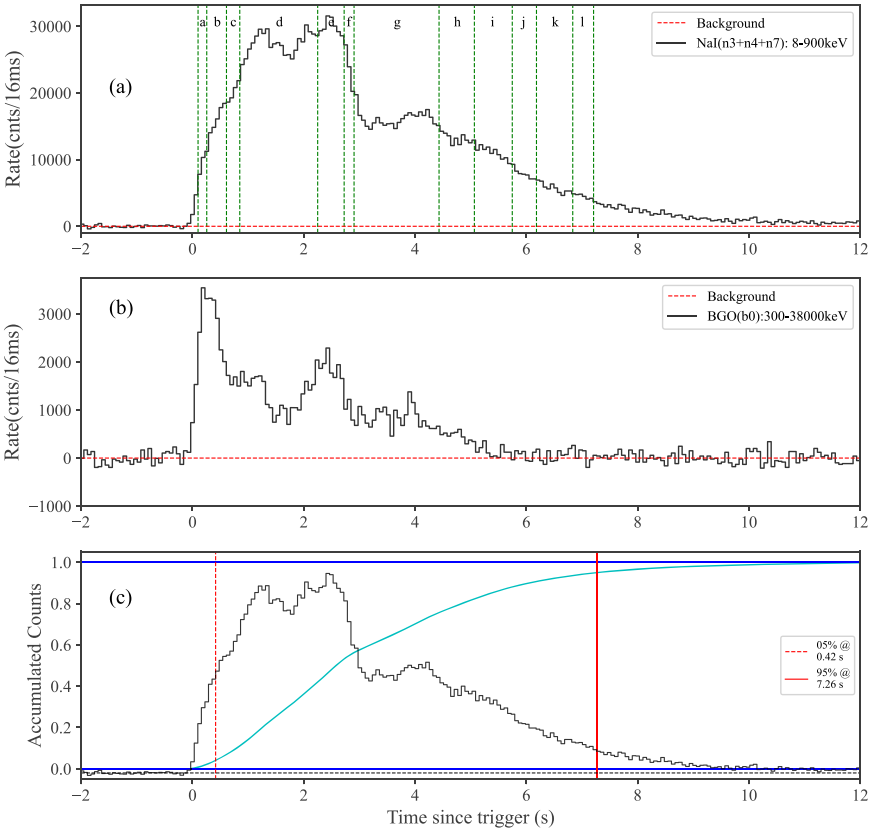

Figure 1. Composite light-curve analysis for GRB 231129C. (a) Shows the light curve from NaI detectors within the 8–900 keV energy range. The green vertical dashed lines in the figure mark the time-resolved regions, while the red horizontal dashed lines represent the background level. (b) Depicts the light curve from BGO detectors within the 300–38,000 keV energy range. (c) Presents the cumulative photon count curve, with the red lines indicating the range of values between 5% and 95% of cumulative photon counts.

In current observations, it is exceedingly rare for a thermal component to dominate and for a complete BB spectrum to be observable. Thus, a more direct evidence akin to "conclusive proof" is the observation of GRB 090902B (Abdo et al. 2009), an exceptionally bright and spectrally narrow GRB. Ryde et al. (2010) confirmed the thermal component within GRB 090902B, finding that this component could be effectively fitted with a multicolor Blackbody (mBB) model. Additionally, it has been suggested that GRB 220426A may also be dominated by thermal emission (Deng et al. 2022; Song et al. 2022; Wang et al. 2022), similar to GRB 090902B, with its spectral fitting indicating that photospheric emission could well describe the spectrum of this burst.

Recently, the Fermi telescope updated online catalog (von Kienlin et al. 2014; Narayana Bhat et al. 2016; von Kienlin et al. 2020) reported a potential thermally dominated burst, GRB 231129C, similar to GRB 090902B and GRB 220426A. Further analysis revealed that both its low-energy and high-energy spectral indices exceed the typical values of normal GRBs, suggesting a narrow spectral feature. In this study, we employed Bayesian methods for the estimation of spectral parameters and model selection, and the results support that a strong photospheric component is present in the spectrum of GRB 231129C.

The structure of this paper is organized as follows: Section 2 presents the observations of GRB 231129C, along with detailed analyses of the time-integrated and time-resolved spectra. Section 3 focuses on the analysis of spectral characteristics. In Section 4, we briefly introduce the GRB models utilized in this study and their specific applications to the GRB 231129C. Additionally, we discuss the composition of GRB jets and the diversity of instantaneous emission characteristics under different scenarios. Section 5 provides a discussion and summary of the findings of this study. Throughout the context, we assume the Hubble constant $H_0 = 70\,\mathrm{km\,s^{-1}\,Mpc^{-1}}$, the matter energy density $\Omega_M = 0.3$, the radiation energy density $\Omega_r = 0$, and the dimensionless cosmological constant $\Omega_\Lambda = 0.7$.

2. Observations and Data Analysis

2.1. Observations

GRB 231129C (trigger 722977823/231129799) successfully triggered the Fermi Gamma-ray Burst Monitor (GBM) and was accurately localized on 2023 November 29, at 19:10:18.11 UT (Sharma et al. 2023). The light curve from Fermi GBM revealed an extremely bright multipeaked pulse structure lasting from T0 + 0 to T0 + 15 s, with the calculated duration T_{90} (within the 50–300 keV range) being approximately 6 s. The fluence measured during this period (within the 10−1000 keV range) was $(8.41 \pm 0.04) \times 10^{-5}\,\mathrm{erg\,cm^{-2}}$. Simultaneously, the Fermi Large Area Telescope also detected the event and further refined its location (Arimoto et al. 2023). Unfortunately, the redshift of this GRB was not measured.

Figure 1 presents the composite light curve of GRB 231129C, integrating data from the NaI (see Figure 1(a)) and BGO (Figure 1(b)) detectors. We recalculated the T_{90} for the NaI detectors within the 50−300 keV energy range, resulting in 6.83 s (shown in Figure 1(c)).

2.2. Data Analysis

The Fermi GBM comprises 12 sodium iodide (NaI) detectors and 2 bismuth germanate (BGO) detectors (Meegan et al. 2009). The NaI detectors span the energy range from 8 keV to 1 MeV, while the BGO detectors cover energies from 200 keV to 40 MeV. Detector selection for analysis is based on their orientation and count rates, leading to the utilization of three NaI detectors (n3, n4, and n7) and one BGO detector (b0) in our study.

Data from the GBM is downloadable through the Fermi Science Support Center via the online Fermi GBM Burst Catalog.[3] Our analysis employed time-tagged event data, featuring 2 ms precision and 128 energy channels, facilitating detailed temporal and spectral resolution analysis. The chosen energy range for the NaI detectors approximately spans from 8 to 900 keV. For the BGO detector, energy channels between 200 keV and 30 MeV were selected. Background for each detector was modeled using polynomial fitting, with polynomials ranging from first to fourth order fitted to intervals before and after the burst, optimizing and retaining the best fit to represent the background.

For the subsequent time-resolved spectral analysis, the brightest NaI detector (n3) is rebinned using Bayesian blocks, setting a false alarm probability at $p_0 = 0.01$ (Scargle et al. 2013). This rebinning yielded 13 time slices (as shown in Figure 1(a)). These selections and fittings were executed using The Multi-Mission Maximum Likelihood package (Vianello et al. 2015).

2.2.1. Spectral Model

The GRBs are often characterized by smoothly joined broken power-law functions, known as the Band function, which is defined as (Band et al. 1993)

$$N(E)_{\rm Band} = A_{\rm Band} \times \begin{cases} \left(\frac{E}{100\ {\rm keV}}\right)^{\alpha} e^{[-E(2+\alpha)/E_{\rm p}]}, & E \leqslant \frac{\alpha-\beta}{2+\alpha}E_{\rm p} \\ \left(\frac{(\alpha-\beta)E_p}{(2+\alpha)100\ {\rm keV}}\right)^{(\alpha-\beta)} e^{(\beta-\alpha)} \left(\frac{E}{100\ {\rm keV}}\right)^{\beta}, & E \geqslant \frac{\alpha-\beta}{2+\alpha}E_{\rm p} \end{cases}, \quad (1)$$

where α and β represent the low-energy and high-energy photon indices, respectively, and $E_{\rm p}$ is the peak energy in the νF_ν spectrum. Furthermore, if the count rate of high-energy photons is relatively low, the high-energy spectral index β may not be well constrained. In such cases, a cutoff power-law (CPL) function can be utilized:

$$N(E)_{\rm CPL} = A_{\rm CPL}\left(\frac{E}{100\ {\rm keV}}\right)^{\alpha} e^{-E/E_{\rm c}}, \quad (2)$$

where α is the photon index and $E_{\rm c}$ is the cutoff energy. The $E_{\rm p}$ of the CPL model is calculated by $E_{\rm c}$, $E_{\rm p} = (2+\alpha) \times E_{\rm c}$. When considering thermal emission, the photon spectrum of blackbody emission is usually expressed as

$$N(E)_{\rm BB} = A_{\rm BB}\frac{E^2}{\exp(E/kT_{\rm BB}) - 1}, \quad (3)$$

where k is the Boltzmann constant and the joint parameter $kT_{\rm BB}$ is the common output parameter.

Typically, the thermal emission spectrum of any astronomical object can be characterized using the Planck function. However, due to the angular dependence of the Doppler effect, the observed blackbody emission temperature varies with the latitude angle. Similar to the case with optical depth, the photosphere radius increases with the angle of observation (Pe'er 2008). This phenomenon similarly affects the angle-dependent density distribution of the outflow. Therefore, compared to a single Planck function, the mBB provides a more accurate description of the photospheric components. By superimposing Planck functions at different temperatures, a phenomenological mBB model can be constructed (see Ryde et al. 2010). The mBB model is extensively employed in spectral fitting for GRBs with thermal spectra (Iyyani & Sharma 2021; Chen et al. 2022; Song et al. 2022, 2024). The mBB model we used has been modified by Hou et al. (2018). The mBB can be expressed as

$$N(E)_{\rm mBB} = \frac{8.0525(m+1)A_{\rm mBB}}{\left[\left(\frac{T_{\rm max}}{T_{\rm min}}\right)^{m+1} - 1\right]}\left(\frac{kT_{\rm min}}{\rm keV}\right)^{-2} I(E),$$
$$I(E) = \left(\frac{E}{kT_{\rm min}}\right)^{m-1} \int_{\frac{E}{kT_{\rm max}}}^{\frac{E}{kT_{\rm min}}} \frac{x^{2-m}}{e^x - 1} dx, \quad (4)$$

where $x = E/kT$, within the temperature range from $kT_{\rm min}$ to $kT_{\rm max}$, the exponent m of the temperature determines the shape of the spectrum. When $m = 2$, the mBB model approximates the spectrum of a pure blackbody emission.

Spectral analysis shows that the spectral widths of many GRBs are actually narrower than those predicted by traditional nonthermal emission models. In particular, in the case of GRB23110C, the observed spectrum exhibits spectral characteristics narrower than generally expected. To explain this phenomenon, we use the nondissipative outflow photosphere (NDP) emission model here, which has the narrowest expected spectral shape. This model was initially proposed by Acuner et al. (2019), and was discussed in detail in their paper. The mathematical representation of the model is as follows:

$$N(E)_{\rm NDP} = A_{\rm NDP}\left(\frac{E}{E_{\rm pivot}}\right)^{0.4} {\rm e}^{-\left(\frac{E}{E_{\rm c}}\right)^{0.65}}, \quad (5)$$

where $E_{\rm pivot}$(set to 100 keV) and $E_{\rm c}$ represent the pivot energy and cutoff energy, respectively, with units of keV. For all the

[3] Data obtained from https://heasarc.gsfc.nasa.gov/W3Browse/fermi/fermigbrst.html.

Table 1
Time-integrated Spectral Fitting Result of GRB 231129C

t_{start}–t_{end} (s)	Model	α	m	β	E_p /E_c (keV)	kT_{min} (keV)	kT/kT_{max} (keV)	$F_{BB} \times 10^{-6}$ (erg cm^{-2} s^{-1})	$F_{Tot} \times 10^{-6}$ (erg cm^{-2} s^{-1})	DIC
0.1 ∼ 8.0	CPL	$-0.32^{+0.01}_{-0.01}$	...	...	$232.68^{+1.61}_{-1.65}$	...	...	...	$9.63^{+9.58}_{-9.67}$	7908.95
	Band	$-0.12^{+0.02}_{-0.02}$	...	$-2.60^{+0.03}_{-0.04}$	$194.71^{+2.98}_{-2.14}$	...	...	...	$10.02^{+0.05}_{-0.05}$	7542.15
	mBB	...	$-0.23^{+0.04}_{-0.02}$	...	...	$10.93^{+0.18}_{-0.30}$	$135.14^{+2.09}_{-3.46}$	...	$9.63^{+0.06}_{-0.06}$	7617.51
	NDP	...	...	...	$28.01^{+0.12}_{-0.13}$	...	...	...	$9.44^{+0.04}_{-0.04}$	7794.46
	CPL+BB	$0.12^{+0.03}_{-0.03}$	...	...	$141.2^{+3.16}_{-3.16}$	...	$113.23^{+2.83}_{-3.19}$	$4.49^{+0.16}_{-0.15}$	$10.18^{+0.06}_{-0.06}$	7275.37
	Band+BB	$0.16^{+0.03}_{-0.02}$	...	$-2.65^{+0.07}_{-0.05}$	$136.70^{+2.22}_{-2.76}$	...	$89.67^{+2.81}_{-2.39}$	$3.12^{+0.17}_{-0.17}$	$10.10^{+0.05}_{-0.05}$	7241.04

aforementioned models, A is the amplitude, with units of ph cm^{-2} keV^{-1} s^{-1}.

To identify the most suitable model from a set of fixed models, we employ the deviance information criterion (DIC) as the selection tool. The criterion is defined as follows:

$$\mathrm{DIC} = -2\log\left[p(\mathrm{data}|\hat{\theta})\right] + 2p_{\mathrm{DIC}}, \quad (6)$$

where p represents the posterior mean of the model, and p_{DIC} is the effective number of parameters. In this paper, given any two estimated models, the preferred model is the one that yields the smallest DIC score.

2.2.2. Time-integrated Spectral Analysis

We applied the aforementioned models and conducted a time-integrated spectral analysis of GRB 231129C using the Markov Chain Monte Carlo (MCMC) method, with the results summarized in Table 1. In the initial phase of the analysis, we employed four non-nested models (Band, CPL, mBB, and NDP) for spectral fitting. Among these, the Band model exhibits the lowest DIC value, indicating it as the best-fit model. Notably, the low-energy spectral indices derived from the Band and CPL models exceed the theoretical limits of the synchrotron emission model, with the high-energy spectral indices surpassing the typical value ($\beta \approx -2.3$, Preece et al. 2000). Subsequently, we introduced a BB model on top of the Band and CPL models, performing spectral fitting with these two nested models. The results show a significant improvement in the goodness of fit upon incorporating the BB component, particularly with the Band+BB model emerging as the optimal model. This suggests a significant thermal component in the spectrum of GRB 231129C. Within the Band+BB model, the total flux F_{Tot} and the flux of the BB component F_{BB} were calculated for the energy range between 10 and 1000 keV, yielding $F_{\mathrm{tot}} = (1.01 \pm 0.01) \times 10^{-5}$ erg cm^{-2} s^{-1} and $F_{\mathrm{BB}} = (3.12 \pm 0.18) \times 10^{-6}$ erg cm^{-2} s^{-1}, respectively, with the BB component accounting for approximately 30.9% of the total energy flux. The peak energy of the Band component is 136.8 keV, while the temperature of the BB component is $kT_{\mathrm{BB}} = 89.5$ keV.

2.2.3. Time-resolved Spectral Analysis

In the detailed time-resolved spectral analysis of GRB 231129C, covering 13 time slices [0.10, 0.26] s, [0.26, 0.61] s, [0.61, 0.85] s, [0.85, 2.25] s, [2.25, 2.73] s, [2.73, 2.90] s, [2.90, 4.43] s, [4.43, 5.07] s, [5.07, 5.75] s, [5.75, 6.18] s, [6.18, 6.83] s, [6.83, 7.21] s, and [7.21, 8.00] s, which are labeled as a to m in Figure 1(a), our analysis results are presented in Table 2, and the evolution of the time-resolved spectral parameters is shown in Figure 2. Initially, we fitted the data from each time interval with two different non-nested models: the Band and CPL models. Our findings indicate that, except for the l and m intervals, the low-energy spectral indices for the remaining intervals exceed the expected limit values of the synchrotron emission model. Particularly, the α values for intervals b, c, and d are relatively high, all above 0. Throughout the entire GRB event, the β value of the Band model was more negative than the typical value of –2.3 (Preece et al. 2000), indicating that the spectrum of this GRB is narrower. This combination of high α values and low β values strongly suggests spectral characteristics similar to those of GRB 090902B, potentially pointing to an origin in photospheric emission.

To further explore the hypothesis of photospheric emission, we also fitted the νF_ν spectra of each time slice with the BB, mBB, and NDP models, with the results shown in Figure 3. By comparing the DIC values of the five non-nested models, as shown in Figure 4(a), we found that the spectra of time slices a, b, e, f, h, i, and j are more inclined to support the NDP model, accounting for 53% (7/13) of the total spectra, providing further evidence for the origin of photospheric emission in GRB 231129C.

Moreover, by introducing a BB component on the Band and CPL models, using nested models Band+BB and CPL+BB for fitting each time slice, we quantitatively determined the photospheric emission component. As shown in Figure 4(b), after the introduction of the BB component, the change of the fitting statistic (ΔDIC) for each time slice is greater than 10, which strongly indicates the significant presence of the BB component. The parameter evolution of these nested models is displayed in Figure 2, where the α values can effectively track the changes in luminosity, and E_p shows a trend from hard to soft, then following the changes in luminosity. Notably, after introducing the BB component, the α values for each time slice become harder, and the peak energy slightly decreases, consistent with the findings of Li (2019).

3. Spectral Characteristics

3.1. $E_{p,z}$–E_{iso} and $T_{90,z}$–EH Correlation

Based on the time-integrated spectral parameters determined in Section 2.2.3, we have compared the performance of GRB 231129C and GRB 090902B in the $E_{p,z}$–E_{iso} relation (Amati et al. 2002), as shown in Figure 5. Due to the lack of precise observations of the redshift, we calculate the $E_{p,z}$–E_{iso} relation for different redshift values (from 0 to 5). For ease of comparison, we also present the case of GRB 090902B, which is predominantly thermal emission, in the figure. Notably, both cases fall within the category of long GRBs. Based on the 1σ

Table 2
Time-resolved Spectral Fitting Result of GRB 231129C

$t_{\rm start} - t_{\rm end}$ (s)	Model	α	m	β	$E_{\rm p}$ /$E_{\rm c}$ (keV)	$kT_{\rm min}$ (keV)	$kT/kT_{\rm max}$ (keV)	$F_{\rm BB} \times 10^{-6}$ (erg cm^{-2} s^{-1})	$F_{\rm Tot} \times 10^{-6}$ erg cm^{-2} s^{-1})	DIC
(a) 0.1 ∼ 0.26	CPL	$-0.03^{+0.06}_{-0.08}$	...	...	$763.17^{+42.65}_{-42.56}$	...	...	...	$20.2^{+19.61}_{-20.78}$	667.29
	Band	$0.01^{+0.07}_{-0.08}$	...	$-3.1^{+0.30}_{-0.19}$	$720.27^{+41.69}_{-45.16}$	...	...	...	$19.83^{+0.56}_{-0.6}$	676.69
	mBB	...	$0.92^{+0.10}_{-0.08}$	...	...	$0.75^{+0.01}_{-3.65}$	$281.23^{+13.26}_{-22.26}$	...	$20.2^{+0.60}_{-0.53}$	681.88
	NDP	...	...	...	$104.38^{+4.0}_{-3.87}$	...	...	...	$19.74^{+0.52}_{-0.54}$	656.25
	BB	...	...	...	...	...	$133.49^{+3.8}_{-3.59}$	...	$21.59^{+0.71}_{-0.71}$	784.49
	CPL+BB	$-0.13^{+0.08}_{-0.14}$	...	...	$806.11^{+88.99}_{-49.27}$	...	$146.58^{+89.2}_{-22.50}$	$1.61^{+1.51}_{-4.14}$	$20.2^{+0.60}_{-0.62}$	653.36
	Band+BB	$-0.07^{+0.15}_{-0.14}$	...	$-2.43^{+0.64}_{-0.02}$	$426.19^{+46.32}_{-288.87}$	...	$196.40^{+38.23}_{-16.92}$	$9.67^{+4.55}_{-3.46}$	$20.32^{+0.64}_{-0.62}$	654.83
(b) 0.26 ∼ 0.61	CPL	$0.13^{+0.04}_{-0.04}$	...	...	$418.18^{+9.71}_{-10.62}$	...	...	...	$21.25^{+20.85}_{-21.63}$	1627.46
	Band	$0.26^{+0.06}_{-0.06}$	...	$-2.93^{+0.25}_{-0.12}$	$376.12^{+13.89}_{-16.37}$	...	...	...	$20.53^{+0.38}_{-0.39}$	1628.06
	mBB	...	$0.07^{+0.07}_{-0.20}$	...	...	$24.01^{+2.48}_{-1.41}$	$211.92^{+16.18}_{-4.71}$	...	$21.25^{+0.37}_{-0.39}$	1613.41
	NDP	...	...	...	$61.54^{+1.15}_{-1.17}$	...	...	...	$21.27^{+0.36}_{-0.37}$	1609.83
	BB	...	...	...	...	...	$82.18^{+1.19}_{-1.21}$	...	$19.85^{+0.39}_{-0.39}$	2061.28
	CPL+BB	$0.57^{+0.11}_{-0.11}$	...	...	$249.24^{+24.41}_{-21.26}$	...	$168.08^{+12.87}_{-12.83}$	$10.79^{+1.77}_{-1.50}$	$21.18^{+0.41}_{-0.40}$	1579.21
	Band+BB	$0.54^{+0.07}_{-0.14}$	...	$-2.9^{+0.24}_{-0.23}$	$246.71^{+23.04}_{-19.69}$	...	$149.05^{+10.25}_{-10.97}$	$9.37^{+1.59}_{-1.42}$	$21.11^{+0.41}_{-0.39}$	1588.26
(c) 0.61 ∼ 0.85	CPL	$0.21^{+0.05}_{-0.05}$	...	...	$265.26^{+6.64}_{-6.22}$	...	...	...	$17.2^{+16.82}_{-17.59}$	1210.59
	Band	$0.44^{+0.08}_{-0.06}$	...	$-2.82^{+0.16}_{-0.10}$	$228.92^{+6.78}_{-8.72}$	...	...	...	$17.54^{+0.35}_{-0.37}$	1180.08
	mBB	...	$-0.54^{+0.27}_{-0.30}$	...	...	$22.66^{+2.02}_{-1.76}$	$157.27^{+18.03}_{-22.04}$	...	$17.2^{+0.4}_{-0.37}$	1201.85
	NDP	...	...	...	$39.84^{+0.78}_{-0.79}$	...	...	...	$18.15^{+0.38}_{-0.38}$	1211.27
	BB	...	...	...	...	...	$54.29^{+0.72}_{-0.85}$	...	$15.52^{+0.3}_{-0.33}$	1471.99
	CPL+BB	$0.47^{+0.05}_{-0.11}$	...	...	$215.48^{+14.67}_{-6.15}$	...	$175.05^{+26.8}_{-17.86}$	$4.35^{+0.90}_{-0.96}$	$17.65^{+0.39}_{-0.40}$	1160.51
	Band+BB	$0.42^{+0.05}_{-0.10}$	...	$-2.82^{+0.16}_{-0.11}$	$229.89^{+12.48}_{-5.47}$	...	$77.03^{+38.78}_{-30.57}$	$0.25^{+0.23}_{-0.85}$	$17.54^{+0.35}_{-0.38}$	1166.4
(d) 0.85 ∼ 2.25	CPL	$0.1^{+0.02}_{-0.02}$	...	...	$211.4^{+1.92}_{-1.81}$	...	...	...	$17.98^{+17.84}_{-18.13}$	3867.83
	Band	$0.32^{+0.03}_{-0.03}$	...	$-2.96^{+0.07}_{-0.05}$	$183.1^{+2.89}_{-2.77}$	...	...	...	$18.52^{+0.14}_{-0.14}$	3699.87
	mBB	...	$-0.41^{+0.11}_{-0.08}$	...	...	$16.30^{+0.47}_{-0.62}$	$118.84^{+3.57}_{-6.00}$	...	$17.98^{+0.16}_{-0.16}$	3709.85
	NDP	...	...	...	$30.16^{+0.22}_{-0.20}$	...	...	...	$18.85^{+0.14}_{-0.15}$	3838.53
	BB	...	...	...	...	...	$43.28^{+0.02}_{-0.11}$	...	$16.27^{+0.08}_{-0.12}$	6815.07
	CPL+BB	$0.47^{+0.04}_{-0.04}$	...	...	$154.67^{+3.07}_{-4.34}$	...	$111.52^{+3.82}_{-5.71}$	$6.1^{+0.44}_{-0.41}$	$18.61^{+0.15}_{-0.15}$	3629.50
	Band+BB	$0.49^{+0.05}_{-0.01}$	...	$-3.15^{+0.15}_{-0.09}$	$153.14^{+0.44}_{-5.95}$	...	$90.28^{+3.66}_{-6.48}$	$4.24^{+0.52}_{-0.42}$	$18.57^{+0.14}_{-0.14}$	3634.79
(e) 2.25 ∼ 2.73	CPL	$-0.19^{+0.02}_{-0.03}$	...	...	$255.85^{+4.40}_{-3.87}$	...	...	...	$21.79^{+21.5}_{-22.1}$	2138.51
	Band	$-0.08^{+0.04}_{-0.03}$	...	$-3.08^{+0.17}_{-0.10}$	$231.86^{+5.73}_{-6.50}$	...	...	...	$21.87^{+0.27}_{-0.27}$	2123.57
	mBB	...	$0.07^{+0.10}_{-0.06}$	...	...	$10.66^{+0.59}_{-0.86}$	$126.25^{+3.41}_{-6.80}$	...	$21.79^{+0.3}_{-0.31}$	2105.99
	NDP	...	...	...	$32.40^{+0.37}_{-0.37}$	...	...	...	$21.75^{+0.26}_{-0.28}$	2077.87
	BB	...	...	...	...	...	$46.18^{+0.39}_{-0.39}$	...	$18.73^{+0.22}_{-0.23}$	4127.60
	CPL+BB	$0.12^{+0.07}_{-0.04}$	...	...	$173.11^{+7.33}_{-13.53}$	...	$124.41^{+6.07}_{-11.95}$	$7.85^{+1.23}_{-1.02}$	$22.21^{+0.31}_{-0.31}$	2068.89
	Band+BB	$0.16^{+0.09}_{-0.02}$	...	$-3.10^{+0.29}_{-0.10}$	$162.85^{+1.06}_{-15.95}$	...	$104.09^{+3.79}_{-9.30}$	$6.84^{+1.08}_{-0.93}$	$22.14^{+0.27}_{-0.28}$	2081.70
(f) 2.73 ∼ 2.9	CPL	$-0.27^{+0.05}_{-0.05}$	...	...	$224.58^{+7.77}_{-7.16}$	...	...	...	$14.32^{+13.94}_{-14.7}$	944.55
	Band	$-0.1^{+0.07}_{-0.08}$	...	$-2.81^{+0.21}_{-0.13}$	$189.84^{+8.79}_{-11.23}$	...	...	...	$14.52^{+0.35}_{-0.36}$	938.74
	mBB	...	$-0.1^{+0.19}_{-0.15}$	...	...	$10.03^{+1.12}_{-1.43}$	$118.84^{+9.02}_{-12.88}$	...	$14.32^{+0.37}_{-0.39}$	948.92
	NDP	...	...	...	$27.47^{+0.6}_{-0.65}$	...	...	...	$14.16^{+0.33}_{-0.35}$	920.53

Table 2
(Continued)

$t_{start} - t_{end}$ (s)	Model	α	m	β	E_p /E_c (keV)	kT_{min} (keV)	kT/kT_{max} (keV)	$F_{BB} \times 10^{-6}$ (erg cm^{-2} s^{-1})	$F_{Tot} \times 10^{-6}$ erg cm^{-2} s^{-1})	DIC
	BB	...	...	...	...	...	$46.38^{+0.02}_{-0.18}$	...	$13.62^{+0.02}_{-0.02}$	1568.68
	CPL+BB	$-0.03^{+0.06}_{-0.12}$	...	...	$168.31^{+14.67}_{-9.14}$	...	$141.01^{+19.63}_{-11.79}$	$4.17^{+0.93}_{-0.89}$	$14.76^{+0.43}_{-0.42}$	910.14
	Band+BB	$-0.02^{+0.09}_{-0.09}$	...	$-2.98^{+0.21}_{-0.21}$	$169.18^{+12.36}_{-16.50}$	...	$118.98^{+33.09}_{-9.53}$	$2.04^{+1.46}_{-1.26}$	$14.68^{+0.35}_{-0.40}$	920.85
(g) 2.9 ∼ 4.43	CPL	$-0.34^{+0.02}_{-0.02}$	...	...	$237.67^{+3.33}_{-3.72}$	...	...	...	$10.54^{+10.42}_{-10.65}$	3590.51
	Band	$-0.27^{+0.03}_{-0.03}$	...	$-3.05^{+0.14}_{-0.13}$	$219.7^{+5.42}_{-5.03}$	...	...	...	$10.7^{+0.12}_{-0.12}$	3574.65
	mBB	...	$0.16^{+0.05}_{-0.06}$	...	...	$7.32^{+0.56}_{-0.5}$	$111.86^{+3.09}_{-3.62}$	...	$10.54^{+0.13}_{-0.13}$	3610.84
	NDP	...	...	...	$28.24^{+0.27}_{-0.28}$	...	...	...	$10.27^{+0.11}_{-0.10}$	3628.39
	BB	...	...	...	...	...	$40.23^{+0.30}_{-0.30}$	...	$8.41^{+0.09}_{-0.08}$	6937.58
	CPL+BB	$-0.17^{+0.03}_{-0.07}$	...	...	$183.27^{+17.42}_{-5.30}$	...	$131.73^{+16.97}_{-6.6}$	$3.02^{+0.60}_{-0.57}$	$10.75^{+0.12}_{-0.13}$	3527.34
	Band+BB	$-0.08^{+0.08}_{-0.03}$	...	$-2.74^{+0.34}_{-0.03}$	$153.18^{+1.79}_{-20.87}$	...	$84.94^{+1.65}_{-13.81}$	$2.86^{+0.62}_{-0.48}$	$10.74^{+0.12}_{-0.12}$	3537.79
(h) 4.43 ∼ 5.07	CPL	$-0.23^{+0.04}_{-0.05}$	...	...	$181.69^{+4.24}_{-4.01}$	...	...	...	$7.02^{+6.89}_{-7.15}$	2172.76
	Band	$-0.09^{+0.06}_{-0.07}$	...	$-2.91^{+0.21}_{-0.11}$	$161.34^{+5.31}_{-6.94}$	...	...	...	$7.36^{+0.14}_{-0.14}$	2168.28
	mBB	...	$0.24^{+0.16}_{-0.11}$	...	...	$6.91^{+0.93}_{-1.24}$	$82.61^{+3.65}_{-5.74}$	...	$7.02^{+0.14}_{-0.15}$	2188.3
	NDP	...	...	...	$23.02^{+0.37}_{-0.38}$	...	...	...	$7.06^{+0.12}_{-0.12}$	2149.07
	BB	...	...	...	...	...	$38.38^{+0.01}_{-0.12}$	...	$6.45^{+0.08}_{-0.06}$	3098.0
	CPL+BB	$-0.05^{+0.07}_{-0.08}$	...	...	$150.98^{+11.55}_{-7.14}$	...	$117.37^{+20.88}_{-9.4}$	$1.56^{+0.44}_{-0.38}$	$7.23^{+0.15}_{-0.16}$	2139.49
	Band+BB	$-0.04^{+0.07}_{-0.08}$	...	$-2.93^{+0.24}_{-0.11}$	$151.88^{+10.62}_{-10.11}$	...	$84.03^{+30.51}_{-7.31}$	$0.51^{+0.44}_{-0.54}$	$7.36^{+0.14}_{-0.14}$	2152.6
(i) 5.07 ∼ 5.75	CPL	$-0.2^{+0.04}_{-0.06}$	...	...	$146.87^{+3.88}_{-3.25}$	...	...	...	$4.90^{+4.80}_{-4.99}$	2110.32
	Band	$-0.1^{+0.06}_{-0.07}$	...	$-3.24^{+0.22}_{-0.14}$	$136.81^{+3.76}_{-4.67}$	...	...	...	$5.15^{+0.11}_{-0.11}$	2115.99
	mBB	...	$0.51^{+0.05}_{-0.13}$	...	...	$3.93^{+2.93}_{-0.61}$	$61.16^{+3.12}_{-1.45}$	...	$4.90^{+0.09}_{-0.09}$	2122.47
	NDP	...	...	...	$19.01^{+0.33}_{-0.34}$	...	...	...	$4.98^{+0.09}_{-0.10}$	2095.8
	BB	...	...	...	...	...	$28.54^{+0.35}_{-0.3}$	...	$4.14^{+0.07}_{-0.07}$	2650.73
	CPL+BB	$-0.10^{+0.10}_{-0.06}$	...	...	$135.12^{+6.25}_{-9.80}$	...	$108.46^{+58.92}_{-0.37}$	$0.42^{+0.38}_{-0.32}$	$4.97^{+0.12}_{-0.13}$	2093.11
	Band+BB	$-0.10^{+0.06}_{-0.07}$	...	$-3.26^{+0.22}_{-0.15}$	$135.95^{+5.6}_{-4.07}$	...	$66.65^{+36.35}_{-4.35}$	$0.07^{+0.06}_{-0.17}$	$5.14^{+0.11}_{-0.11}$	2102.76
(j) 5.75 ∼ 6.18	CPL	$-0.36^{+0.07}_{-0.10}$	...	...	$123.28^{+4.99}_{-4.9}$	...	...	...	$2.97^{+2.88}_{-3.07}$	1508.72
	Band	$-0.27^{+0.08}_{-0.10}$	...	$-3.05^{+0.29}_{-0.14}$	$115.4^{+5.14}_{-5.03}$	...	...	...	$3.2^{+0.11}_{-0.11}$	1513.62
	mBB	...	$0.41^{+0.09}_{-0.10}$	...	...	$0.71^{+0.13}_{-2.02}$	$51.48^{+2.74}_{-2.63}$	...	$2.97^{+0.09}_{-0.09}$	1518.09
	NDP	...	...	...	$15.30^{+0.40}_{-0.42}$	...	...	...	$2.97^{+0.08}_{-0.08}$	1500.65
	BB	...	...	...	...	...	$27.61^{+0.01}_{-0.11}$	...	$2.74^{+0.08}_{-0.05}$	1791.94
	CPL+BB	$-0.27^{+0.13}_{-0.05}$	...	...	$114.18^{+3.60}_{-10.57}$	...	$92.46^{+58.81}_{-0.0}$	$0.12^{+0.11}_{-0.25}$	$3.01^{+0.09}_{-0.11}$	1493.41
	Band+BB	$-0.27^{+0.09}_{-0.10}$	...	$-3.04^{+0.32}_{-0.10}$	$114.25^{+5.57}_{-4.95}$	...	$44.82^{+18.04}_{-19.39}$	$0.04^{+0.03}_{-0.10}$	$3.20^{+0.10}_{-0.11}$	1501.12
(k) 6.18 ∼ 6.83	CPL	$-0.57^{+0.08}_{-0.08}$	...	...	$113.27^{+5.06}_{-4.84}$	...	...	...	$2.02^{+1.95}_{-2.08}$	1921.89
	Band	$-0.48^{+0.1}_{-0.09}$	...	$-3.04^{+0.26}_{-0.20}$	$106.44^{+5.07}_{-5.20}$	...	...	...	$2.17^{+0.08}_{-0.09}$	1927.37
	mBB	...	$0.17^{+0.2}_{-0.06}$	...	...	$0.89^{+0.07}_{-3.12}$	$50.24^{+2.12}_{-5.27}$	...	$2.02^{+0.06}_{-0.07}$	1934.23
	NDP	...	...	...	$13.16^{+0.37}_{-0.37}$	...	...	...	$1.94^{+0.05}_{-0.05}$	1925.66
	BB	...	...	...	...	...	$25.68^{+0.01}_{-0.12}$	...	$1.81^{+0.03}_{-0.03}$	2304.97
	CPL+BB	$-0.47^{+0.14}_{-0.05}$	...	...	$101.01^{+2.9}_{-13.05}$	...	$88.36^{+55.23}_{-2.98}$	$0.1^{+0.09}_{-0.19}$	$2.04^{+0.07}_{-0.08}$	1906.43
	Band+BB	$-0.53^{+0.05}_{-0.14}$	...	$-3.01^{+0.29}_{-0.16}$	$107.13^{+8.51}_{-2.92}$	...	$44.3^{+17.86}_{-16.78}$	$0.03^{+0.03}_{-0.08}$	$2.18^{+0.08}_{-0.08}$	1914.29

Table 2
(Continued)

$t_{\rm start}-t_{\rm end}$ (s)	Model	α	m	β	$E_{\rm p}$ /$E_{\rm c}$ (keV)	$kT_{\rm min}$ (keV)	$kT/kT_{\rm max}$ (keV)	$F_{\rm BB}\times10^{-6}$ (erg cm^{-2} s^{-1})	$F_{\rm Tot}\times10^{-6}$ erg cm^{-2} s^{-1})	DIC
(l) 6.83 $\sim$ 7.21	CPL	$-0.72^{+0.11}_{-0.14}$	...	...	$100.48^{+7.34}_{-6.77}$	...	...	...	$1.45^{+1.38}_{-1.52}$	1198.85
	Band	$-0.66^{+0.1}_{-0.18}$	...	$-2.78^{+0.35}_{-0.16}$	$94.21^{+8.85}_{-6.51}$	...	...	...	$1.6^{+0.08}_{-0.09}$	1202.89
	mBB	...	$0.04^{+0.40}_{-0.06}$	...	...	$0.65^{+0.31}_{-4.07}$	$45.82^{+2.23}_{-11.49}$	...	$1.45^{+0.06}_{-0.07}$	1211.32
	NDP	...	...	...	$11.25^{+0.48}_{-0.48}$	...	...	...	$1.35^{+0.05}_{-0.06}$	1199.82
	BB	...	...	...	...	...	$23.71^{+0.03}_{-0.30}$	...	$1.28^{+0.03}_{-0.04}$	1384.73
	CPL+BB	$-0.61^{+0.18}_{-0.10}$	...	...	$89.41^{+5.25}_{-12.72}$	...	$84.18^{+52.95}_{-5.54}$	$0.07^{+0.06}_{-0.16}$	$1.47^{+0.07}_{-0.09}$	1183.87
	Band+BB	$-0.63^{+0.14}_{-0.16}$	...	$-2.90^{+0.24}_{-0.27}$	$91.57^{+9.34}_{-6.74}$	...	$46.83^{+19.86}_{-15.72}$	$0.03^{+0.03}_{-0.08}$	$1.61^{+0.08}_{-0.09}$	1189.64
(m) 7.21 $\sim$ 8.0	CPL	$-0.89^{+0.09}_{-0.14}$	...	...	$81.67^{+5.25}_{-5.03}$	...	...	...	$0.85^{+0.81}_{-0.89}$	1983.89
	Band	$-0.79^{+0.14}_{-0.18}$	...	$-2.73^{+0.36}_{-0.16}$	$74.63^{+6.44}_{-6.38}$	...	...	...	$0.95^{+0.05}_{-0.05}$	1987.00
	mBB	...	$-0.35^{+0.28}_{-0.18}$	...	...	$3.18^{+1.59}_{-1.11}$	$45.05^{+4.22}_{-10.97}$	...	$0.85^{+0.04}_{-0.04}$	1996.92
	NDP	...	...	...	$9.07^{+0.38}_{-0.38}$	...	...	...	$0.78^{+0.03}_{-0.03}$	1993.05
	BB	...	...	...	...	...	$16.39^{+0.1}_{-0.5}$	...	$0.67^{+0.02}_{-0.02}$	2156.38
	CPL+BB	$-0.82^{+0.14}_{-0.14}$	...	...	$75.09^{+6.53}_{-7.91}$	...	$60.83^{+32.58}_{-3.87}$	$0.04^{+0.04}_{-0.08}$	$0.86^{+0.04}_{-0.04}$	1969.05
	Band+BB	$-0.78^{+0.12}_{-0.19}$	...	$-2.77^{+0.32}_{-0.19}$	$73.28^{+8.60}_{-5.22}$	...	$53.76^{+29.29}_{-1.82}$	$0.02^{+0.02}_{-0.05}$	$0.95^{+0.05}_{-0.06}$	1973.36

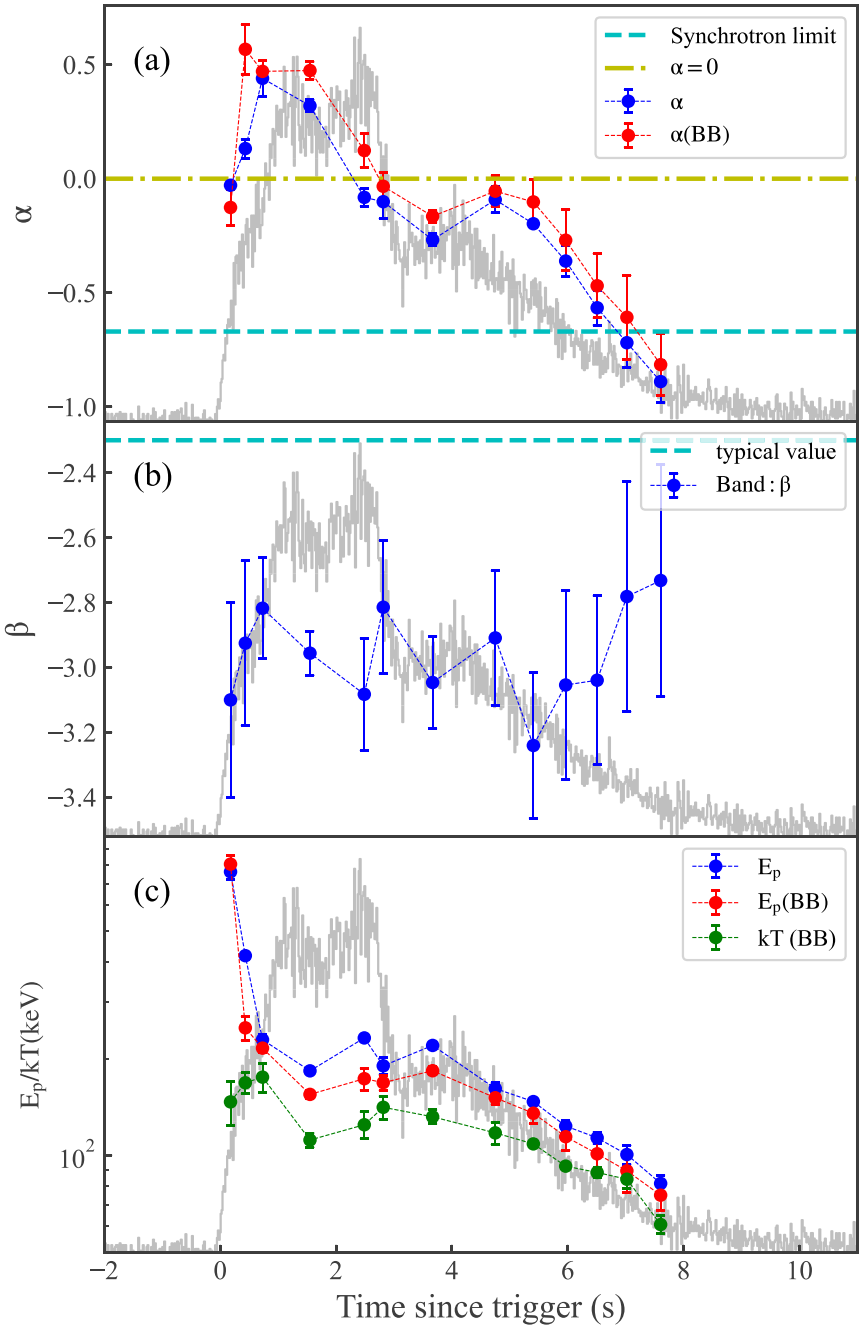

Figure 2. The parameters of the time-resolved spectrum evolve over time. Panel (a) shows how the low-energy spectral index α evolves over time, where blue and red markers represent cases without and with the inclusion of a BB component, respectively. The cyan and yellow dashed lines indicate the synchrotron "death line" and $\alpha = 0$, respectively. Panel (b) demonstrates how the peak energy E_p changes over time, with green markers representing the blackbody temperature. The (c) panel displays the evolution of the high-energy spectral index β over time, where the cyan dashed line represents the typical value $\beta = -2.3$.

confidence interval for long GRBs in the $E_{p,z}$–E_{iso} relation, we estimate the redshift of GRB 231129C to be about 0.5.

In addition to the Amati relation, Minaev & Pozanenko (2020) proposed a classification scheme that combines the correlation between E_{iso} and $E_{p,z}$, as well as the bimodal distribution of T_{90}. To describe the correlation between $E_{p,z}$ and E_{iso}, they suggest using the Energy-Hardness (EH) parameter,

$$\mathrm{EH} = \frac{(E_{p,z}/100\mathrm{keV})}{(E_{iso}/10^{51}\mathrm{erg})^{0.4}}. \quad (7)$$

Figure 5(b) shows the $T_{90,z}$–EH trajectory of GRB 231129C calculated for different redshifts (from 0 to 5). Similarly, this relationship can be used to estimate the redshift (Minaev & Pozanenko 2020). As shown in the figure, when the redshift $z = 0.5$, the trajectory lies within the 1σ confidence interval.

3.2. T_{90}-related Correlation

We analyzed various correlations and distributions related to T_{90} to identify the characteristics of GRB 231129C. Specifically, we explored the relationships between T_{90} and hardness ratio (HR), T_{90} and peak energy E_p, as well as T_{90} and α. Here, HR is defined as the ratio of observed counts in the 50–300 keV range to those in the 10–50 keV range, while both E_p and α of each burst are taken from the Fermi GBM catalog

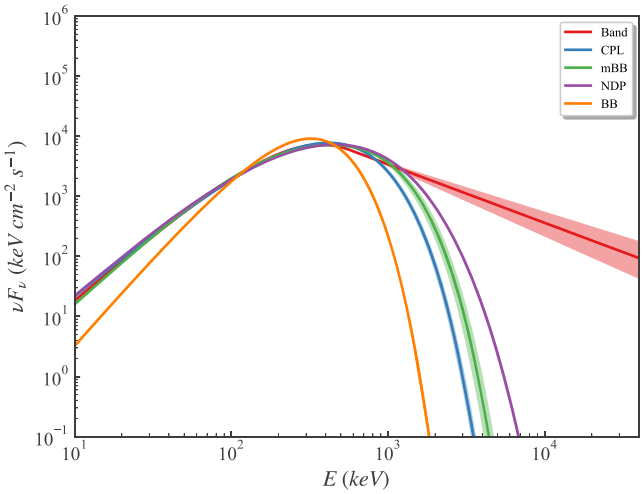

Figure 3. The νF_ν spectrum of time slice b in the time-resolved spectrum, showing the fitting results for the Band, CPL, BB, mBB, and NDP models.

(von Kienlin et al. 2014). In Figure 6, we compared the performance of GRB 231129C and GRB 090902B in T_{90}–HR, T_{90}–E_p, and T_{90}–α with other bursts in the catalog. The classification of these two types of bursts was obtained by fitting with a Bayesian Gaussian mixture model using `scikitlearn` (Pedregosa et al. 2011).

From Figure 6(a), GRB 231129C has a harder spectrum than GRB 090902C. Further analysis of the peak energy E_p of the two bursts in Figure 6(b) shows that GRB 231129C has a significantly lower peak energy than GRB 090902B. This observation contradicts the conclusions of Liang et al. (2002), who suggested that harder spectra usually have higher peak energies, a finding also supported by Shahmoradi & Nemiroff (2010), indicating a strong positive correlation between the HR and peak energy. However, in our comparison, GRB 231129C exhibits a higher hardness but a lower peak energy, indicating different spectral indices between the two bursts.

From Figure 6(c), the low-energy spectral indices of the time-integrated spectra of both bursts are greater than the synchrotron death line, and the low-energy spectral index of GRB 231129C is harder than that of GRB 090902B, which implies that the harder spectrum is steeper (Liang et al. 2002). The hard low-energy spectral indices of GRB 231129C and GRB 090902B can be explained by the nondissipative photospheric emission model (Pe'er et al. 2012; Acuner et al. 2019; Ahlgren et al. 2019).

3.3. Correlation of Spectral Parameters

Building on the time-resolved spectral analysis obtained in Section 2.2.3, we conduct a statistical analysis of the best model parameters for each time slice. Figure 7 shows the interrelationships between the spectral parameters α, E_p, kT, and the flux (F). Specifically, a notable correlation between α and F is shown in Figure 7(a), with a Spearman correlation coefficient R of 0.868. For the α–F relation, Ryde et al. (2019) define the relation as a log-linear function: $F = F_0 e^{k\alpha}$, where F_0 is the normalized factor. They found the value of parameter k to be approximately 3. In the case of GRB 231129C, we also observed a similar linear relationship, with a k value of 3.00 ± 0.10 obtained through MCMC fitting. Our results are consistent with those of Ryde et al. (2019), suggesting that the α–F relationship may be indicative of subphotospheric heating in outflows with varying entropy. Higher entropy brings the photosphere closer to the saturation radius, resulting in intense radiation and narrow spectra. As entropy decreases, the photosphere recedes from the saturation radius, and weaker radiation and broader spectra are expected (for a detailed discussion, see Ryde et al. 2019).

In extensive GRB research, the E_p–F relationship has been identified not only in the overall spectra of multiple GRBs but also in the time-resolved spectral analysis of individual GRBs (Wei & Gao 2003; Lu et al. 2012), and this relationship can be naturally explained by the photosphere model (Fan et al. 2012; Deng & Zhang 2014). However, the E_p–F data sample of GRB 231129C shows significant inflection behavior, as depicted in Figure 7(b). In this study, we used a smooth inflection law function to fit the E_p–F data sample, expressed as

$$F(E_p) = F_0 \left[\left(\frac{E_p}{E_b} \right)^{k_1} + \left(\frac{E_p}{E_b} \right)^{k_2} \right]^{-1}. \quad (8)$$

Based on the analysis of the optimal model sample, we determined the best-fit inflection energy E_p to be 200.22 ± 0.10 keV, the first segment slope k_1 as -3.50 ± 0.10, and the second segment slope k_2 as -0.08 ± 0.02. Furthermore, a strong positive correlation between kT and F was also observed, as shown in Figure 7(c), with a Spearman correlation coefficient R value reaching 0.82. This relation can be accurately described by the equation $F/(\mathrm{erg\ cm^{-2}\ s^{-1}}) = 10^{-12}(kT/\mathrm{keV})^{3.30\pm0.01}$.

4. Properties of the Photosphere Emission

Through detailed spectral analysis results, we are able to investigate the properties of the outflows in GRB 231129C. Various observational results indicate that the composition of jets may differ between each GRB. This also raises the possibility of the existence of hybrid jets, where the jets contain both thermal and magnetized components, and the level of magnetization varies (Hascoët et al. 2013; Gao & Zhang 2015). In this work, we focus on two methods that allow for the study of outflows that may simultaneously possess thermal and magnetic components.

The first framework, developed by Hascoët et al. (2013), has subsequently been applied to the study of jet properties in some GRBs (Guiriec et al. 2013, 2015; Arimoto et al. 2016; Siddique et al. 2022). We refer to this method as the HDM2013 method. The second framework, developed by Gao & Zhang (2015), is used to study outflows and has been employed to constrain parameters of the GRB photospheric emission. We refer to this method as the GZ2015 method. It is important to note that neither of these methods includes dissipation in the subphotospheric layer. In this study, we utilize these two methods to investigate the photospheric properties of GRB 231129C.

4.1. The HDM2013 Method

In the HDM2013 method, the initial power injected into the outflow exists partially in the form of thermal energy ($\epsilon_{\rm Th}$) at the initial radius (R_0), with the remainder existing in the form of magnetic energy ($1 - \epsilon_{\rm Th}$). For a pure fireball model, $\epsilon_{\rm Th} \simeq 1$; whereas for cases dominated by Poynting flux, $\epsilon_{\rm Th} \to 0$. The acceleration of the outflow can be driven by thermal energy, magnetic energy, or a combination of both. The outflow forms a spherical shape at the radius $R_{\rm sph}$ and

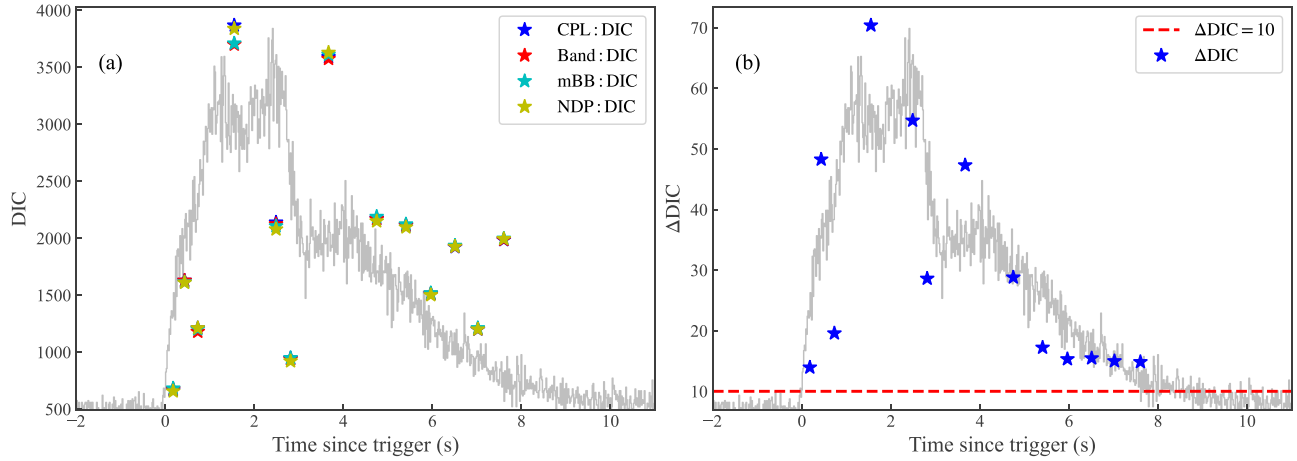

Figure 4. In the analysis of the time-resolved spectrum, the trend of DIC over time. Panel (A) presents in detail the DIC results obtained by fitting with the Band, CPL, BB, mBB, and NDP models within each time slice. Panel (B), on the other hand, shows the change in DIC ($\Delta\mathrm{DIC} = \mathrm{DIC} - \mathrm{DIC_{BB}}$) before and after the introduction of a BB component at each time point, where the red dashed line marking $\Delta\mathrm{DIC} = 10$ serves as a criterion, indicating that an actual ΔDIC exceeding this line means that the inclusion of the BB component has significantly improved the fit of the model.

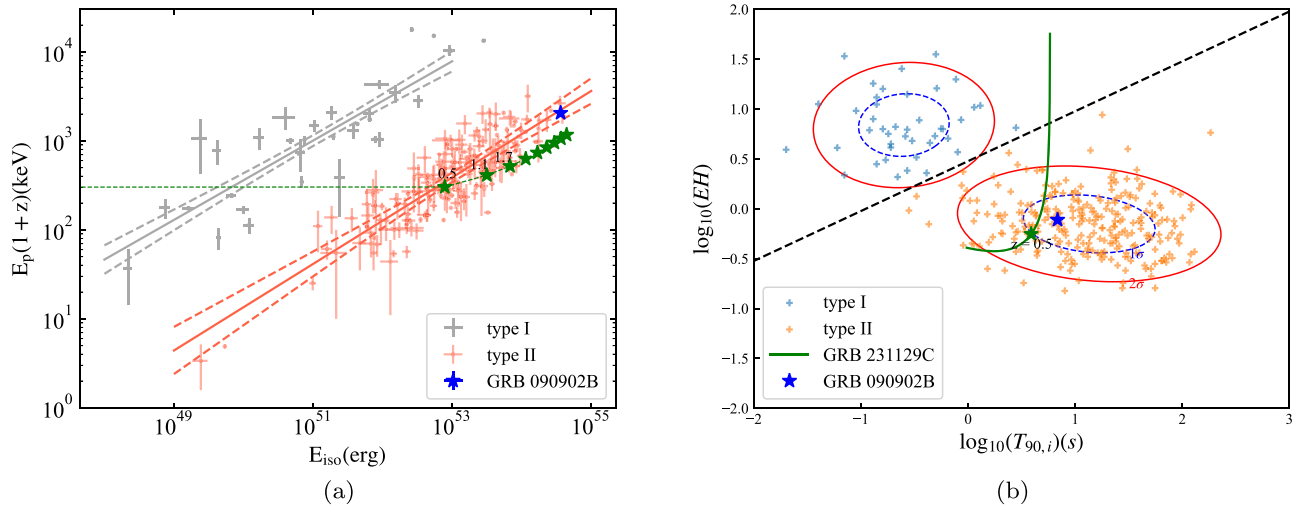

Figure 5. The $E_{p,z}$–E_{iso} and $T_{90,z}$–EH relation. Panels (a) is the intrinsic spectral peak energy ($E_{p,z}$) and an isotropic equivalent gamma-ray radiation energy (E_{iso}) correlation diagram. The gray and red dashed lines represent the best-fit correlations for the Type I and Type II GRB samples, respectively. Panel (b) shows the $T_{90,z}$–EH diagram, where the blue dashed line and the red solid line represent the 1σ and 2σ confidence ellipses, respectively, and the green star indicates the position of GRB 231129C at a redshift of $z = 0.5$. Green and purple stars represent GRB 231129C and GRB 090902B, respectively. The green trajectory indicates GRB 231129C at different redshift values (from 0.0 to 5.00).

completes its acceleration at the saturation radius R_{sat}, satisfying $R_{sat} > R_{sph}$. At the photosphere radius R_{ph}, the outflow becomes transparent, allowing thermal photons to be emitted. In this framework, it is generally assumed that $R_{sat} < R_{ph}$, and there is no magnetic dissipation below the photosphere. At the end of the acceleration phase, the magnetization strength σ of the outflow corresponds to the ratio of magnetic flux to kinetic energy flux. Hascoët et al. (2013) introduced the concept of passive magnetization strength $\sigma_{passive} \simeq (1-\epsilon_{Th})/\epsilon_{Th}$, which should not be exceeded by σ at the end of outflow acceleration. If $\sigma \ll \sigma_{passive}$, it indicates efficient magnetic acceleration of the outflow; whereas if $\sigma \approx \sigma_{passive}$, the outflow is primarily accelerated by thermal energy.

Guiriec et al. (2013) extended the method proposed by Pe'er et al. (2007) to magnetized outflows based on the (Hascoët et al. 2013) theoretical framework. In this scenario, the expressions for the initial radius R_0, the Lorentz factor Γ, and the photosphere radius R_{ph} can be reformulated as follows:

$$R_0 \simeq \left[\frac{D_L \mathcal{R}}{2(1+z)^2}\left(\frac{\phi}{1-\phi}\right)^{3/2}\right] \times \left[\frac{f_{NT}}{\epsilon_{Th}}\right]^{3/2}, \quad (9)$$

$$\Gamma \simeq \left[\frac{\sigma_T}{m_p c^3}\frac{(1+z)^2 D_L F_{BB}}{\mathcal{R}}\frac{1-\phi}{\phi}\right]^{1/4} \times [(1+\sigma) f_{NT}]^{-1/4}, \quad (10)$$

$$R_{ph} \simeq \left[\frac{\sigma_T}{16 m_p c^3}\frac{D_L^5 F_{BB} \mathcal{R}^3}{(1+z)^6}\frac{1-\phi}{\phi}\right]^{1/4} \times [(1+\sigma) f_{NT}]^{-1/4}. \quad (11)$$

The parameter $\mathcal{R}$ is given by Pe'er et al. (2007),

$$\mathcal{R} = \left(\frac{F_{BB}}{\sigma_{SB} T_{BB}^4}\right)^{1/2}. \quad (12)$$

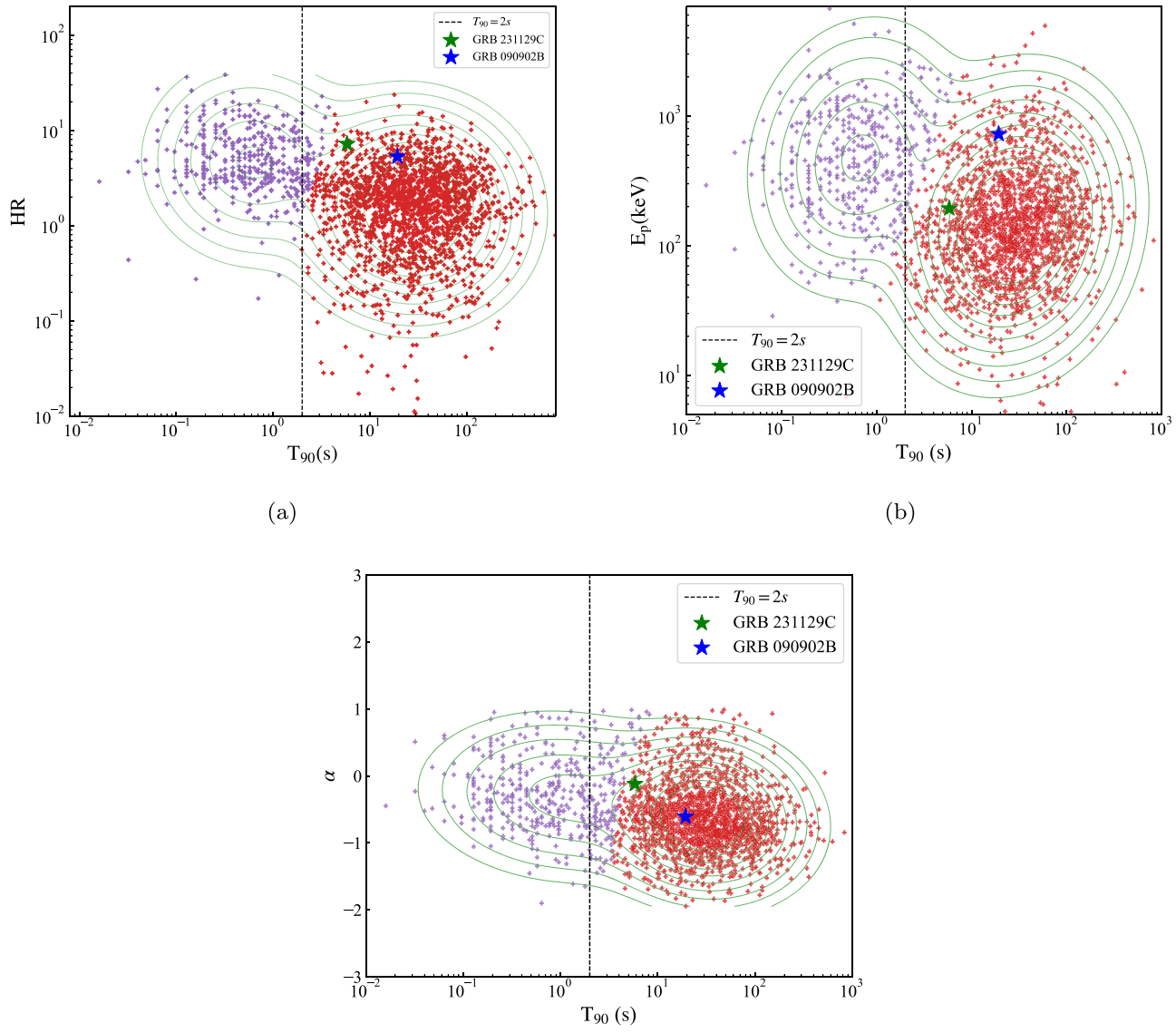

Figure 6. Statistical distribution comparison of peak energy E_p, HR, and α. Panels (a), (b), and (c) respectively show the relationship between T_{90} and HR, T_{90} and E_p, and T_{90} and α, comparing them with the Fermi catalog and other bursts. Blue points represent Type I GRB samples, and red points represent Type II GRB samples.

In the above equations, D_L represents the luminosity distance, while F_{BB} stands for the observed flux of the BB component. The ratio $\phi = F_{BB}/F_{Tot}$ denotes the proportion of the observed BB component flux to the total observed flux F_{Tot}. Additionally, z is the redshift of the GRB, σ_T is the Thomson scattering cross section, m_p denotes the proton mass, and c represents the speed of light. σ_{SB} is the Stefan–Boltzmann constant, and T_{BB} is the observed temperature. These observational values are detailed in the spectral fitting results in Section 2.2.2.

We use Equations (9)–(11) to estimate the values of these parameters. Since the redshift of GRB 231129C is unknown we adopt the redshift estimated in Section 3.1, $z = 0.5$. The calculated results are presented in Table 3.

We estimate the initial radius (R_0) of GRB 231129C using the parameter values obtained through time-integrated analysis. According to Equation (9), we calculate R_0 as $(1.27 \pm 0.18) \times 10^8 \times (f_{NT}/\epsilon_{Th})^{3/2}$ cm. Figure 8(a) shows the dependency of R_0 on f_{NT}/ϵ_{Th} (black line) for GRB 231129C. As the ratio of f_{NT}/ϵ_{Th} increases, R_0 correspondingly increases. Referring to assumptions made by Siddique et al. (2022) regarding R_0, we set $R_0 = 2.1 \times 10^6$ cm, 10^7 cm, and 10^8 cm. For these radius values, we then apply Equation (9) in reverse to determine the corresponding f_{NT}/ϵ_{Th} values (see Table 3). From Figure 8(a), it can be observed that the range of f_{NT}/ϵ_{Th} ratios corresponding to these three radius values spans from 0.06 to 0.85. As shown in Figure 8(b), we present the relationship between f_{NT} and ϵ_{Th}, and provide the range of magnetization values for $f_{NT} = 0.5$, 0.1, and 0.05 (as shown in Figure 8(c)). These parameter values allow us to explore various scenarios of nonthermal emission processes. When $f_{NT} = 0.5$, the occurrence of internal shocks is considered unlikely, which is consistent with efficient magnetic reconnection processes. When $f_{NT} = 0.1$, it may be consistent with either magnetic reconnection or efficient internal shock processes. However, when $f_{NT} = 0.05$, the magnetic reconnection process is considered unlikely. The values of f_{NT}, ϵ_{Th}, and $\sigma_{passive}$

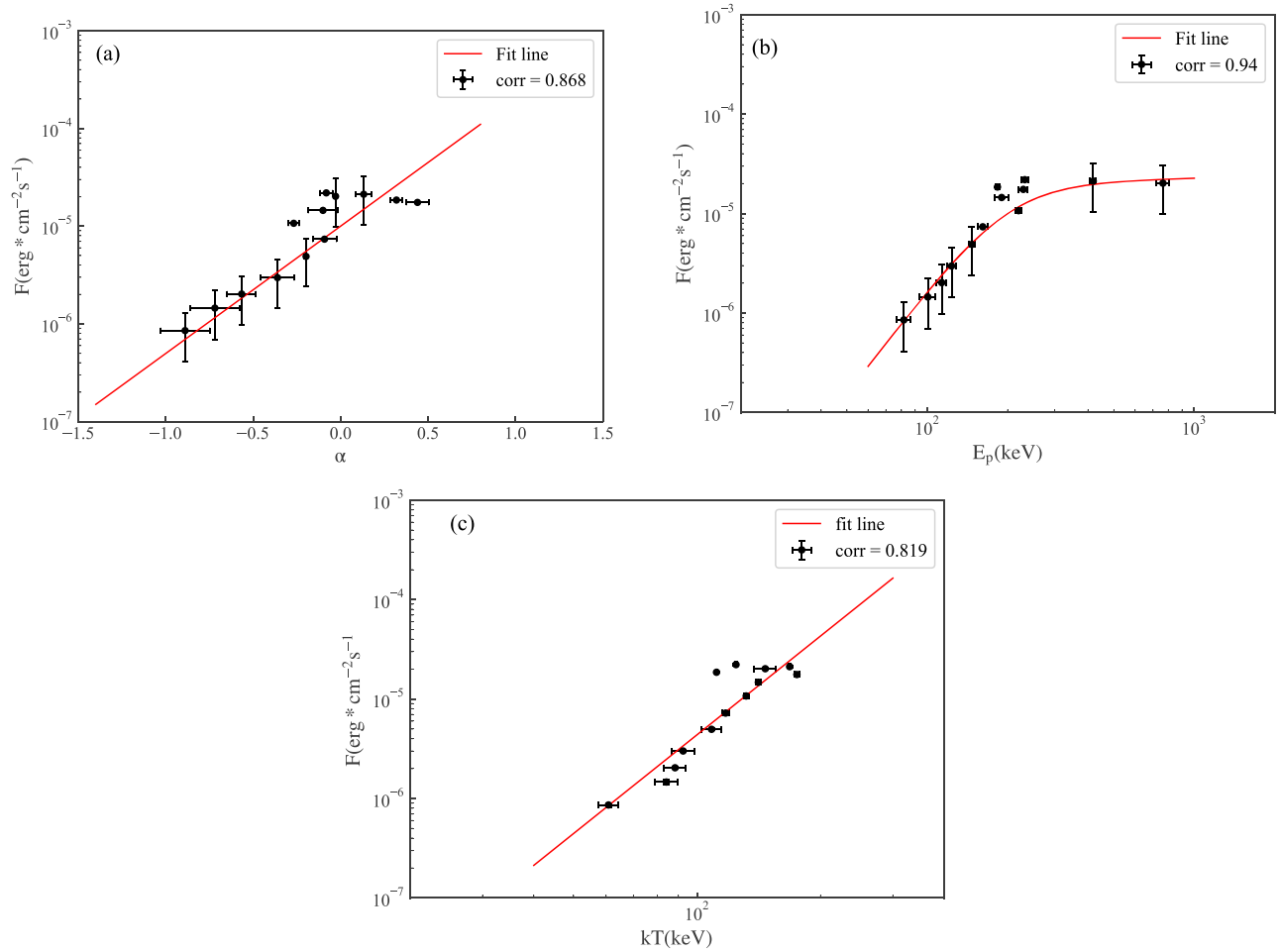

Figure 7. The α–F relationship (panel a), the F–E_p relationship (panel (b)), and the F–kT relationship (panel (c)) of the best model sample for GRB 232219C. The red lines represent the best-fit lines of the model. Additionally, we have labeled the correlation coefficients (corr).

corresponding to each R_0 are given in Table 4. Based on these results, we can discuss the following different physical scenarios:

(1) When $R_0 = 2.1 \times 10^6$ cm, the pure fireball model is applicable to GRB 231129C. As mentioned above, the pure fireball model requires $\epsilon_{\rm Th} \simeq 1$ and $\sigma \simeq 0$. It is noted that within the range of nonthermal emission efficiency from 0.06 to 0.1, these conditions are met. Moreover, when the nonthermal emission efficiency $f_{\rm NT} > 0.1$, it also meets the conditions of the pure fireball model ($\epsilon_{\rm Th} \simeq 1$, $\sigma \simeq 0$). However, high-efficiency nonthermal processes are only possible in the case of magnetic reconnection, which cannot occur in the pure fireball model. Therefore, at a small radius ($R_0 = 2.1 \times 10^6$ cm), the possibility of magnetic reconnection is excluded.

(2) When $R_0 = 10^7$ cm and $f_{\rm NT} = 0.5$, we obtain $\epsilon_{\rm Th} \simeq 1$, indicating that the nonthermal emission process might be magnetic reconnection, which is impossible in the pure fireball model. For $f_{\rm NT} = 0.1$, $\epsilon_{\rm Th} \simeq 0.55$, and $\sigma_{\rm passive} \simeq 0.83$, suggesting that thermal emission dominates at R_0, and nonthermal emission processes may tend toward internal shocks. For $f_{\rm NT} = 0.05$, the expected internal shocks are more likely, with an initial thermal fraction of 0.27, and $\sigma_{\rm passive} \simeq 2.67$, indicating that the initial outflow is magnetically dominated. Efficient magnetic acceleration would result in $\sigma << 1$, allowing for the generation of internal shocks. If such low efficiency can also be associated with magnetic reconnection, the outflowing magnetic acceleration needs to be relatively inefficient to achieve $\sigma > 1$ and allow for magnetic reconnection.

(3) When $R_0 = 10^8$ cm, for the case of high efficiency $f_{\rm NT} = 0.5$, the initial thermal fraction $\epsilon_{\rm Th} \simeq 0.59$, leading to $\sigma_{\rm passive} \simeq 0.70$, which is less than 1, indicating insufficient magnetization at the end of the acceleration phase for magnetic reconnection. Hence, this scenario is ruled out. For $f_{\rm NT} = 0.10$, the initial thermal fraction is 0.1, and $\sigma_{\rm passive}$ is 7.51, implying that at $R_0 = 10^8$ cm, the outflow is dominated by Poynting flux. After acceleration, if magnetic acceleration is inefficient and the outflow acceleration is provided by the initial thermal fraction, then magnetic reconnection is possible. If most of the initial magnetic energy is converted into kinetic energy, then high-efficiency internal shocks (where high-efficiency internal shocks correspond to $f_{\rm NT} = 0.1$) are also possible instead of magnetic reconnection. For $f_{\rm NT} = 0.50$, with an initial thermal fraction of 0.05, $\sigma_{\rm passive}$ value is 16.03, suggesting that if magnetic acceleration is efficient, internal shocks are possible. If magnetic acceleration is inefficient ($\sigma > 1$), magnetic reconnection can be a nonthermal emission process.

4.2. The GZ2015 Method

Gao & Zhang (2015) introduced the magnetization parameter σ_0 on the basis of the traditional fireball model, defined as $\sigma_0 = L_{\rm c}/L_{\rm b}$, where $L_{\rm b}$, $L_{\rm c}$, and $L_0 = L_{\rm c} + L_{\rm b}$ represent the thermal component, the Poynting flux component, and the total

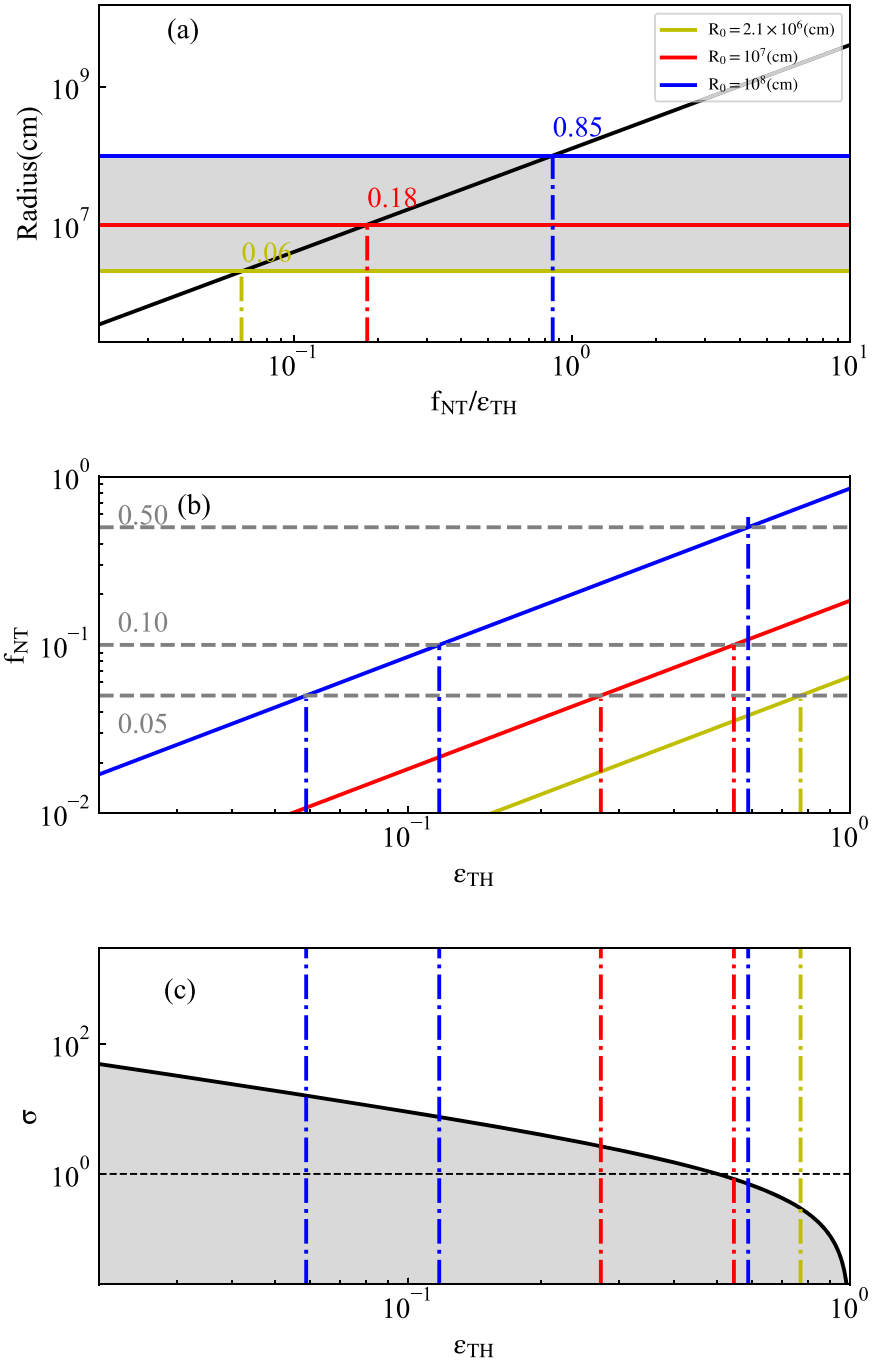

Figure 8. Panel (a) Based on the time-integrated analysis results of GRB 231129C, the dependence of f_{NT}/ϵ_{Th} on R_0 is shown (solid lines). The yellow, red, and blue solid lines represent $R_0 = 2.1 \times 10^6$ cm, 10^7 cm, and 10^8 cm, respectively, with intersections with the black solid line determining the values of f_{NT}/ϵ_{Th}. Panel (b) Shows the nonthermal emission efficiency f_{NT} as a function of initial thermal fraction ϵ_{Th} for three initial radii. Three horizontal lines correspond to $f_{NT} = 0.5$, 0.1, and 0.05. For each f_{NT} value, the corresponding initial thermal fraction ϵ_{Th} for a given initial radius is indicated by vertical lines (specific values can be found in Table 3). Panel (c) According to the HDM2013 method, the magnetization factor σ at the end of acceleration is shown by the black curve, with the limit $\sigma_{passive} = (1 - \epsilon_{Th})/\epsilon_{Th}$ depicted by the shadow region where $\sigma < \sigma_{passive}$. Vertical dashed lines correspond to the ϵ_{Th} values for $f_{NT} = 0.5$, 0.1, and 0.05.

luminosity of the entire wind, respectively. Consequently, the rapid evolution of the emission characteristics of the photosphere is believed to be the result of the rapid evolution of σ and η (the dimensionless entropy of the outflow). Similar to the approach in Hascoët et al. (2013), this method also allows for the simultaneous presence of magnetic and thermal components at the onset of the outflow. In this method, the acceleration of the jet is initially dominated by thermal acceleration ($r_0 < r < r_a$), entering a phase of rapid acceleration until reaching the rapid acceleration radius r_a. Subsequently, a slow acceleration phase dominated by magnetic acceleration ($r_a < r < r_s$) begins, continuing until the saturation radius r_s. Finally, it enters a coasting phase ($r > r_s$). Therefore, for the rapid acceleration phase, the acceleration law can be approximated as $\Gamma \propto r$. For the slow acceleration phase, it can be expressed as $\Gamma \propto r^{\delta}$, where $0 < \delta \leqslant \frac{1}{3}$ (Mészáros & Rees 2011; Veres & Mészáros 2012). In the coasting phase, the acceleration law is $\Gamma = \Gamma_c$. Due to the photosphere radius r_{ph}

Table 3
Magnetization Factor, Initial Thermal Fraction, and Dimensionless Entropy among Other Parameters Calculated by the HDM2013 and GZ2015 Methods

Radius	f_{NT}/ϵ_{TH}	HDM2013						GZ2015				
		ϵ_{TH}			$\sigma_{passive}$			Regime	$1+\sigma_0$	η	$1+\sigma_{ph}$	$1+\sigma_{15}$
$\times 10^7$ cm		$f_{NT}=0.5$	0.1	0.05	$f_{NT}=0.5$	0.1	0.05					
0.21	0.06	1.00	1.00	0.77	0.00	0.00	0.30	III	1.00	2139.09	...	...
1	0.18	1.00	0.55	0.27	0.00	0.83	2.67	III	1.00	755.74	...	...
10.00	0.85	0.59	0.12	0.06	0.70	7.51	16.03	III	2.11	162.82	...	...

Table 4
Outflow Characteristic Parameters Calculated by the HDM2013 and GZ2015 Methods

Parameter	
HDM2013 Method	
$\mathcal{R} \times 10^{-19}$	2.17 ± 0.17
$R_0 \times 10^8 [f_{NT}/\epsilon_{Th}]^{3/2}$ cm	1.27 ± 0.18
$\Gamma \times [(1+\sigma) f_{NT}]^{-1/4}$	311.61 ± 59.97
$R_{ph} \times 10^{11} [(1+\sigma) f_{NT}]^{-1/4}$ cm	1.32 ± 0.25
GZ2015 Method	
Γ_{ph}	343.99 ± 27.55
$R_{ph} \times 10^{11}$ cm	2.87 ± 0.23

being dividable into three distinct regions separated by r_{ra} and r_c, there are two possible values for the Lorentz factor Γ_{ra} at r_{ra} for different central engine parameters: $\eta > (1+\sigma)^{1/2}$ and $\eta < (1+\sigma)^{1/2}$. Hence, there are six distinct regions for the properties of the photosphere in the hybrid system: Region I: $\eta > (1+\sigma)^{1/2}$ and $r_{ph} < r_{ra}$; Region II: $\eta > (1+\sigma)^{1/2}$ and $r_{ra} < r_{ph} < r_c$; Region III: $\eta > (1+\sigma)^{1/2}$ and $r_{ph} > r_c$; Region IV: $\eta < (1+\sigma)^{1/2}$ and $r_{ph} < r_{ra}$; Region V: $\eta < (1+\sigma)^{1/2}$ and $r_{ra} < r_{ph} < r_c$; and Region VI: $\eta < (1+\sigma)^{1/2}$ and $r_{ph} > r_c$.

Gao & Zhang (2015) proposed a "top-down" approach to diagnose central engines, which evaluates the situation of GRBs and calculates parameters of the outflow based on observed values of F_{BB}, kT, and F_{Tot}. However, introducing the magnetization parameter σ_0 into the hybrid jet model leads to four unknown parameters of the central engine (L_w, R_0, η, and σ_0), making it difficult to directly solve from observational data. To address this issue, Gao & Zhang (2015) suggest analyzing them based on the assumption of a constant R_0. Additionally, apart from R_0, knowledge of the ratio f_γ of gamma-ray luminosity to total wind luminosity is required. With these assumptions, all characteristic parameters of the hybrid model's photosphere can be obtained, including η, $1+\sigma_0$, r_{ph}, Γ_{ph}, $1+\sigma_{ph}$, and $1+\sigma_{15}$, where r_{ph} is the photosphere radius, Γ_{ph} is the Lorentz factor at r_{ph}, $1+\sigma_{ph}$ is the magnetization parameter at r_{ph}, and $1+\sigma_{15}$ is the magnetization parameter at 10^{15} cm.

We applied the GZ2015 method to GRB 231129C. Similar to the HDM2013 method, we assume the initial radii R_0 of the jet to be 2.1×10^6 cm, 10^7 cm, and 10^8 cm, while setting $f_\gamma = 0.5$. Based on the results of time-integrated spectral analysis, including F_{BB}, kT, and F_{Tot}, we first select regions according to the judgment criteria provided in Table 2 of Gao & Zhang 2015, then calculate the physical parameters of the hybrid jet model using the corresponding formulas. The computed results are shown in Table 4.

First, it is noteworthy that for all three initial radii (2.1×10^6 cm, 10^7 cm, and 10^8 cm), GRB 231129C is classified into the third region identified by Gao & Zhang (2015), indicating that the acceleration ends before the photosphere radius, consistent with the assumption in Hascoët et al. (2013). For $R_0 = 2.1 \times 10^6$ cm and 10^7 cm, we obtain $\sigma_0 = 0$ and $\eta >> 1$, suggesting a pure fireball. This result aligns with the findings of the HDM2013 method for $R_0 = 2.1 \times 10^6$ cm and $f_{NT} = 0.06-0.1$. When $R_0 = 10^8$ cm, $(1+\sigma_0) \simeq 2.11$, and $\eta >> 1$, indicating that besides the thermal fireball component, the cold Poynting flux component may also play a significant role in the GRB, consistent with the analysis results of the HDM2013 method. Additionally, we observe that η decreases as R_0 increases.

Continuing, we calculate the photosphere emission parameters for each time slice using the results of the time-resolved spectra analysis. In the time-resolved spectra, for $R_0 = 2.1 \times 10^6$ cm and 10^7 cm, all time slices fall into the third region identified by Gao & Zhang (2015). As shown in Figure 9, we present the photosphere characteristic parameters. Consistent with the analysis results of time-integrated spectra, $(1+\sigma_0) \simeq 1$ and $\eta >> 1$ for all time slices, indicating compatibility with the thermal fireball model. Li (2020) applied the GZ2015 method to analyze GRB 090902B, and from their analysis results, it can be seen that when $R_0 = 10^7$ cm, there also exists $(1+\sigma_0) \simeq 1$ and $\eta >> 1$. This suggests that GRB 231129C is similar to GRB 090902B, both dominated by thermal emission.

When $R_0 = 1 \times 10^8$ cm, most time slices are split between the third and second regions, with the majority falling into the third region. Furthermore, for most time slices, the magnetization factor $(1+\sigma_0) > 1$, consistent with the analysis results of the time-integrated spectra, indicating the importance of the cold Poynting flux component besides the thermal component. In the time slices belonging to the second region, we can compute the magnetization factor at the photosphere and at a radius of 10^{15} cm. Through these calculations, we find that $(1+\sigma_{ph}) > 1$, while $(1+\sigma_{15}) \simeq 1$, indicating that the outflow has entered the coasting phase and internal shocks are the mechanism for nonthermal emission production, similar to the case of GRB 090902B.

5. Discussion and Conclusion

In this study, we utilize observations from Fermi GBM during the prompt emission phase and conduct a detailed spectral analysis of GRB 231129C using Bayesian and MCMC methods. Initially, we perform time-integrated spectral analysis using four models: Band, CPL, mBB, and NDP, and find that GRB 231129C differs from most GRBs, exhibiting extremely hard low-energy spectral indices and very soft high-energy spectral indices, suggesting a possible dominance of thermal mission. Subsequently, incorporating the BB model onto the Band and CPL models, we observe significant improvement in fitting.

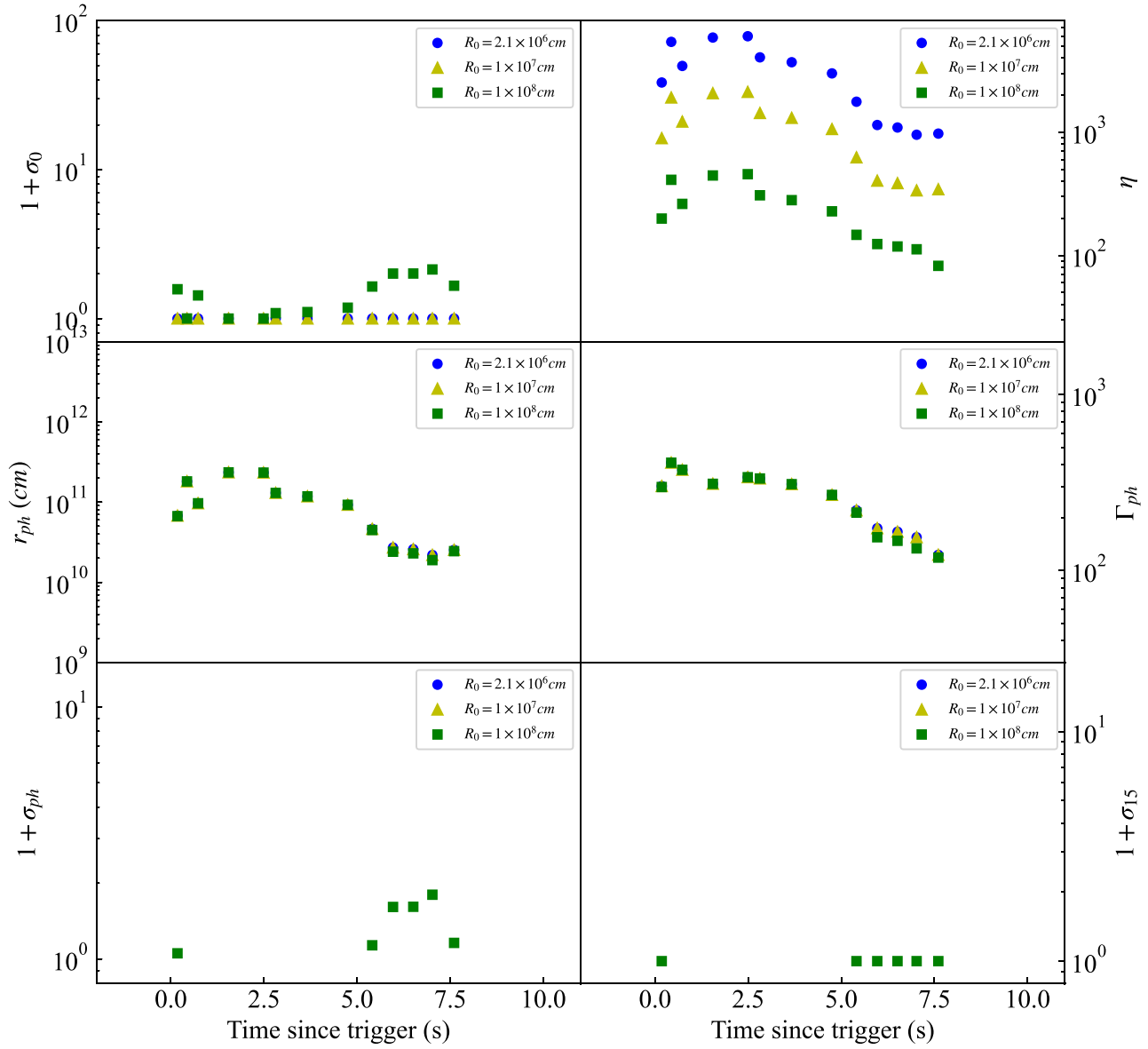

Figure 9. The evolution of the photosphere parameters ($1+\sigma_0$, η, $r_{\rm ph}$, $\Gamma_{\rm ph}$, $1+\sigma_{\rm ph}$, $1+\sigma_{15}$) calculated using the GZ2015 method over time. The blue, yellow, and green symbols represent the photosphere emission parameters calculated at initial radii of $R_0 = 2.1 \times 10^6$ cm, 10^7 cm, and 10^8 cm, respectively.

Further time-resolved spectral analysis reveals that 92% of the time slices have low-energy spectral indices exceeding the limit of synchrotron emission, known as the "line of death," with the hardest spectral index $\alpha \sim +0.44$. In optically thick thermal scenarios, $\alpha = 1$ at the Rayleigh–Jeans limit and $\alpha = 2$ at the Wien limit. However, due to geometric effects, spectral deviations from Planck spectra broaden the spectral shape, with the expected spectral index α for nondissipative photospheres during the coasting phase being approximately +0.4 (Goodman 1986; Pe'er 2008; Beloborodov 2010). However, Acuner et al. (2019) analyzed synthetic spectra from a nondissipative photosphere, folding the theoretical predictions through the detector response matrix of the Fermi GBM detector. They found that when the simulated spectra are fitted with the usual empirical models, the obtained values of the low-energy photon indices are $-0.4 < \alpha < 0.0$, proving that GRBs with a spectral index greater than -0.4 are compatible with photospheric emission from nondissipative outflows. They also suggested that one should not expect to obtain hard α values from photospheric emission, such as $\alpha = 1$ (Rayleigh–Jeans slope) or $\alpha = 0.4$ (including geometrical effects), because the empirical models used for spectral analysis (Band and CPL models) do not fully capture the true curvature of the theoretical spectrum.

In the time-resolved spectra of GRB 231129C, 10 time slices (*a–j*) had α values greater than –0.4, and the time-integrated spectrum had an α value of –0.12, which is also greater than –0.4. Our analysis results are consistent with the predicted values, indicating that the first 6.2 s of GRB 231129C can originate from a nondissipative photosphere. Additionally, we employ the NDP model proposed by Acuner et al. (2019) for spectral fitting, and find that 53% (7/13) of the spectra can be well fitted, further supporting the photospheric origin.

Furthermore, detailed time-integrated and time-resolved spectral analysis results enable us to compute values describing the central engine and outflow parameters. We employ both HDM2013 and GZ2015 methods, which allow us to investigate jets simultaneously comprising thermal and

nonthermal components, using observed BB fluxes, total fluxes, and BB temperatures.

We assume three different initial radii for the jet: $R_0 = 2.1 \times 10^6$ cm, 10^7 cm, and 10^8 cm. First, using the HDM2013 method, we investigate potential physical scenarios for GRB 231129C under these different radii. We find that at smaller initial radii (2.1×10^6 cm), a pure fireball model is applicable for the burst when the nonthermal emission efficiency is between 0.06 and 0.1, as at this point the thermal emission efficiency ($\epsilon_{\rm Th}$) is 1 and the magnetization parameter (σ) is 0. This differs from the analysis of Nawaz & Sajjad (2022) and Siddique et al. (2022) for GRB 150902A and GRB130518A, where they reject pure fireball models and efficient magnetic reconnection at small radii. However, our analysis results suggest that a pure fireball model is feasible for GRB 231129C at small radii. When using the GZ2015 method, for $R_0 = 2.1 \times 10^6$ cm and 10^7 cm we similarly obtain $\sigma_0 \simeq 0$ and $\eta >> 1$, implying a thermal fireball model. At moderate radii (10^7 cm), pure fireball and efficient magnetic reconnection are ruled out in line with their analysis results. At larger radii ($R_0 = 10^8$ cm), the scenario with a nonthermal emission efficiency of 0.5 is excluded. Low-efficiency magnetic reconnection may be possible at nonthermal emission efficiencies of 0.05–0.1, but this would require very low-efficiency magnetic acceleration.

In summary, our detailed analysis of GRB 231129C reveals the following characteristics:

(1) In both time-integrated and time-resolved spectral analyses, the low-energy spectral index exceeds the so-called synchrotron "line of death," with the hardest $\alpha \sim +0.44$, consistent with the expected value for the coasting phase of a nondissipative photosphere. Meanwhile, the high-energy spectral index is more negative than the typical value ($\beta \sim -2.3$). This implies that GRB 231129C shares a narrow spectral feature with GRB 090902B.

(2) 53% (7/13) of the spectra can be well fitted by the nondissipative photosphere model.

(3) GRB 231129C and GRB 090902B exhibit consistency in $E_{\gamma,\rm iso}-E_{\rm p,z}$, $T_{90}-$HR, and $T_{90}-E_{\rm p}$ distributions, both being long GRBs with $E_{\rm p}$ in the hundreds of keV range.

(4) The low-energy spectral index displays an intensity-tracking evolution pattern, with the $\alpha-F$ relationship organized as $F = F_0 10^{3.00\pm0.10\alpha}$, and the variation in dimensionless entropy η provides a natural explanation for this correlation (Ryde et al. 2019). The peak energy $E_{\rm p}$ also exhibits a strong correlation with the flux; however, unlike most GRBs, GRB 231129C's $E_{\rm p}-F$ relationship shows a broken behavior, well described by a smoothly bending power-law function. The blackbody temperature (kT) also shows a strong correlation with the flux, described by $F/(\rm erg\ cm^{-2}\ s^{-1}) = 10^{-12}(kT/\rm keV)^{(3.30\pm0.01)}$.

(5) A pure fireball model is applicable for GRB 231129C at smaller initial radii.

Acknowledgments

We acknowledge the use of the public data from the Fermi data archives. This work is supported by the National Natural Science Foundation of China (NSFC 12233006 and 12163007), the Yunnan University graduate research innovation fund project KC-23233826, and the Scientific Research Fund of Education Department of Yunnan Province (2024Y036).

ORCID iDs

Jia-Ming Chen https://orcid.org/0000-0001-5681-6939
Ke-Rui Zhu https://orcid.org/0000-0002-3132-1507
Zhao-Yang Peng https://orcid.org/0000-0003-3846-0988
Li Zhang https://orcid.org/0000-0002-7824-4289

References

Abdo, A. A., Ackermann, M., Ajello, M., et al. 2009, ApJL, 706, L138
Acuner, Z., Ryde, F., & Yu, H.-F. 2019, MNRAS, 487, 5508
Ahlgren, B., Larsson, J., Ahlberg, E., et al. 2019, MNRAS, 485, 474
Amati, L., Frontera, F., Tavani, M., et al. 2002, A&A, 390, 81
Arimoto, M., Asano, K., Ohno, M., et al. 2016, ApJ, 833, 139
Arimoto, M., Omodei, N., Kocevski, D. & Fermi-LAT Collaboration 2023, GCN, 35238, 1
Asano, K., & Terasawa, T. 2009, ApJ, 705, 1714
Band, D., Matteson, J., Ford, L., et al. 1993, ApJ, 413, 281
Beloborodov, A. M. 2010, MNRAS, 407, 1033
Chen, J.-M., Peng, Z.-Y., Du, T.-T., & Yin, Y. 2022, ApJ, 932, 25
Daigne, F., Bošnjak, Ž., & Dubus, G. 2011, A&A, 526, A110
Deng, L.-T., Lin, D.-B., Zhou, L., et al. 2022, ApJL, 934, L22
Deng, W., & Zhang, B. 2014, ApJ, 785, 112
Fan, Y.-Z., Wei, D.-M., Zhang, F.-W., & Zhang, B.-B. 2012, ApJL, 755, L6
Gao, H., & Zhang, B. 2015, ApJ, 801, 103
Geng, J.-J., Huang, Y.-F., Wu, X.-F., Zhang, B., & Zong, H.-S. 2018, ApJS, 234, 3
Ghirlanda, G., Celotti, A., & Ghisellini, G. 2003, A&A, 406, 879
Ghirlanda, G., Pescalli, A., & Ghisellini, G. 2013, MNRAS, 432, 3237
Ghisellini, G., Celotti, A., & Lazzati, D. 2000, MNRAS, 313, L1
Goodman, J. 1986, ApJL, 308, L47
Guiriec, S., Connaughton, V., Briggs, M. S., et al. 2011, ApJL, 727, L33
Guiriec, S., Daigne, F., Hascoët, R., et al. 2013, ApJ, 770, 32
Guiriec, S., Gehrels, N., McEnery, J., Kouveliotou, C., & Hartmann, D. H. 2017, ApJ, 846, 138
Guiriec, S., Mochkovitch, R., Piran, T., et al. 2015, ApJ, 814, 10
Hascoët, R., Daigne, F., & Mochkovitch, R. 2013, A&A, 551, A124
Hou, S.-J., Zhang, B.-B., Meng, Y.-Z., et al. 2018, ApJ, 866, 13
Iyyani, S., Ryde, F., Ahlgren, B., et al. 2015, MNRAS, 450, 1651
Iyyani, S., Ryde, F., Burgess, J. M., Pe'er, A., & Bégué, D. 2016, MNRAS, 456, 2157
Iyyani, S., & Sharma, V. 2021, ApJS, 255, 25
Kobayashi, S., Ryde, F., & MacFadyen, A. 2002, ApJ, 577, 302
Kobayashi, S., & Sari, R. 2001, ApJ, 551, 934
Kumar, P. 1999, ApJL, 523, L113
Kumar, P., & Zhang, B. 2015, PhR, 561, 1
Li, L. 2019, ApJS, 245, 7
Li, L. 2020, ApJ, 894, 100
Liang, E.-W., Xie, G.-Z., & Rong, X.-G. 2002, Ap&SS, 280, 357
Lu, R.-J., Wei, J.-J., Liang, E.-W., et al. 2012, ApJ, 756, 112
Meegan, C., Lichti, G., Bhat, P. N., et al. 2009, ApJ, 702, 791
Mészáros, P. 2019, MmSAI, 90, 57
Meszaros, P., & Rees, M. J. 1993, ApJ, 405, 278
Mészáros, P., & Rees, M. J. 2000, ApJ, 530, 292
Mészáros, P., & Rees, M. J. 2011, ApJL, 733, L40
Minaev, P. Y., & Pozanenko, A. S. 2020, MNRAS, 492, 1919
Narayana Bhat, P., Meegan, C. A., von Kienlin, A., et al. 2016, ApJS, 223, 28
Nawaz, A., & Sajjad, S. 2022, MNRAS, 516, 4180
Paczynski, B. 1990, ApJ, 363, 218
Paczyński, B. 1998, ApJL, 494, L45
Pedregosa, F., Varoquaux, G., Gramfort, A., et al. 2011, JMLR, 12, 2825
Pe'er, A. 2008, ApJ, 682, 463
Pe'er, A., Ryde, F., Wijers, R. A. M. J., Mészáros, P., & Rees, M. J. 2007, ApJL, 664, L1
Pe'er, A., Zhang, B. B., Ryde, F., et al. 2012, MNRAS, 420, 468
Piran, T., Shemi, A., & Narayan, R. 1993, MNRAS, 263, 861
Preece, R. D., Briggs, M. S., Giblin, T. W., et al. 2002, ApJ, 581, 1248
Preece, R. D., Briggs, M. S., Mallozzi, R. S., et al. 2000, ApJS, 126, 19
Rees, M. J., & Meszaros, P. 1994, ApJL, 430, L93
Ryde, F. 2004, ApJ, 614, 827
Ryde, F., Axelsson, M., Zhang, B. B., et al. 2010, ApJL, 709, L172
Ryde, F., Kocevski, D., Bagoly, Z., Ryde, N., & Mészáros, A. 2005, A&A, 432, 105
Ryde, F., & Pe'er, A. 2009, ApJ, 702, 1211
Ryde, F., Yu, H.-F., Dereli-Bégué, H., et al. 2019, MNRAS, 484, 1912

Scargle, J. D., Norris, J. P., Jackson, B., & Chiang, J. 2013, ApJ, 764, 167
Shahmoradi, A., & Nemiroff, R. J. 2010, MNRAS, 407, 2075
Sharma, V., Fletcher, C., Meegan, C. & Fermi Gamma-ray Burst Monitor Team 2023, GCN, 35227, 1
Shemi, A., & Piran, T. 1990, ApJL, 365, L55
Siddique, I., Sajjad, S., & Motiwala, K. 2022, ApJ, 938, 159
Song, X.-Y., Wang, L.-J., & Zhang, S. 2024, ApJ, 961, 137
Song, X.-Y., Zhang, S.-N., Ge, M.-Y., & Zhang, S. 2022, MNRAS, 517, 2088
Uhm, Z. L., & Zhang, B. 2014, NatPh, 10, 351
Veres, P., & Mészáros, P. 2012, ApJ, 755, 12
Vianello, G., Lauer, R. J., Younk, P., et al. 2015, arXiv:1507.08343
von Kienlin, A., Meegan, C. A., Paciesas, W. S., et al. 2014, ApJS, 211, 13
von Kienlin, A., Meegan, C. A., Paciesas, W. S., et al. 2020, ApJ, 893, 46
Wang, X.-Y., Li, Z., Dai, Z.-G., & Mészáros, P. 2009, ApJL, 698, L98
Wang, Y., Zheng, T.-C., & Jin, Z.-P. 2022, ApJ, 940, 142
Wei, D. M., & Gao, W. H. 2003, MNRAS, 345, 743
Zhang, B. 2018, The Physics of Gamma-Ray Bursts (Cambridge: Cambridge Univ. Press)
Zhang, B. 2020, NatAs, 4, 210
Zhang, B., & Pe'er, A. 2009, ApJL, 700, L65
Zhang, B., & Yan, H. 2011, ApJ, 726, 90